

A Novel 3D Beam Domain Channel Model for UAV Massive MIMO Communications

Hengtai Chang¹, Member, IEEE, Cheng-Xiang Wang², Fellow, IEEE, Ji Bian³, Member, IEEE, Rui Feng⁴, Member, IEEE, Yubei He⁵, Student Member, IEEE, Yunfei Chen⁶, Senior Member, IEEE, and El-Hadi M. Aggoune⁷, Life Senior Member, IEEE

Abstract—Due to the agile maneuverability, unmanned aerial vehicles (UAVs) have shown great promise for on-demand communications in the next-generation wireless networks. Considering the massive multiple-input multiple-output (MIMO) configuration, this paper proposes a novel three-dimensional (3D) beam domain channel model (BDCM) for UAV communications. Through dividing the large antenna array into several sub-arrays and classifying multipath components as near-field and far-field components, the proposed BDCM takes the spherical wave front (SWF) and array non-stationarity into account. Channel statistical properties including spatial-temporal-frequency correlation function (STF-CF), root-mean-squared (RMS) Doppler spread, beam spread, channel matrix collinearity (CMC), and stationary time interval are derived and simulated for the proposed BDCM. Influences of SFW and non-stationary properties on

the statistical properties and system performance are analyzed. Simulation results show that, compared with the equivalent geometry-based stochastic model (GBSM), the proposed BDCM has better temporal correlation, while BDCM and GBSM are equivalent in the system performance evaluation. Furthermore, the performance of the proposed BDCM is evaluated in terms of accuracy, complexity, and pervasiveness. The results show that the proposed BDCM can represent massive MIMO channel properties accurately with low complexity and good compatibility.

Index Terms—Unmanned aerial vehicles, massive MIMO, non-stationary channel model, GBSM, BDCM.

I. INTRODUCTION

THE unmanned aerial vehicle (UAV) communication is a key enabling technology for the beyond fifth-generation (B5G) and sixth-generation (6G) wireless communication systems [1], [2], [3], [4], [5]. Equipped with the light airborne base station (ABS), UAVs can provide wireless access for ground users (GUs) in UAV assisted-communications [6]. Due to the advantage of flexible deployment, compared with conventional terrestrial communications using static BSs, the UAV assisted-communication is especially appealing for on-demand communication scenarios, such as temporary or unexpected events, emergency response, and search and rescue [7]. On the other hand, to fulfil the increasing demand for capacity, high-speed, full coverage, and to suppress severe interference caused by dominant line-of-sight (LoS) UAV channels, massive multiple-input multiple-output (MIMO) is considered as a practical solution due to its numerous merits, such as improved spectral efficiency and energy efficiency, and high resolution beamforming [8], [9]. With the increase of antenna element number, plane wave front (PWF) and array domain wide sense stationary (WSS) assumptions of traditional MIMO channels are no longer valid as the expansion of near-field region, which makes traditional channel models not applicable [10]. In this case, UAV channel models assuming spherical wave front (SWF) and non-stationary properties become indispensable for the design and evaluation of massive MIMO UAV communication technologies.

So far, there have been a lot of works on UAV channel modeling and massive MIMO channel modeling. For UAV channel modeling, researchers mainly concentrate on time-varying channel characteristics caused by the three-dimensional (3D) UAV trajectory/posture and variation of channel properties at different altitudes [11]. To capture the Doppler effect and temporal non-stationarity caused by the change of UAV and

Manuscript received 21 June 2022; revised 29 October 2022; accepted 17 December 2022. Date of publication 10 January 2023; date of current version 14 August 2023. This work was supported in part by the National Key Research and Development Program of China under Grant 2018YFB1801101; in part by the National Natural Science Foundation of China (NSFC) under Grant 61960206006 and Grant 62101311; in part by the Key Technologies Research and Development Program of Jiangsu (Prospective and Key Technologies for Industry) under Grant BE2022067, Grant BE2022067-3, and Grant BE2022067-1; in part by the Research Fund of National Mobile Communications Research Laboratory, Southeast University, under Grant 2021B02; in part by the European Union (EU), Horizon2020 (H2020), Research and Innovation Staff Exchange (RISE), Testing and Evaluating Sophisticated information and communication Technologies for enaBling scalable smart grid Deployment (TESTBED2) Project under Grant 872172; in part by the Distinguished Postdoctoral Program in Jiangsu; in part by King Abdullah University of Science and Technology Research Funding (KRF) under Award ORA-2021-CRG10-4696; and in part by the University of Tabuk, Saudi Arabia, under Grant S-1443-001. The associate editor coordinating the review of this article and approving it for publication was J. Hamalainen. (Corresponding author: Cheng-Xiang Wang.)

Hengtai Chang and Rui Feng are with the Purple Mountain Laboratories, Nanjing 211111, China, and also with the School of Information Science and Engineering, Southeast University, Nanjing 210096, China (e-mail: changhengtai@pmlabs.com.cn; fengrui@pmlabs.com.cn).

Cheng-Xiang Wang is with the National Mobile Communications Research Laboratory, School of Information Science and Engineering, Southeast University, Nanjing 210096, China, and also with the Purple Mountain Laboratories, Nanjing 211111, China (e-mail: chxwang@seu.edu.cn).

Ji Bian is with the School of Information Science and Engineering, Shandong Normal University, Jinan, Shandong 250399, China (e-mail: jibian@sdu.edu.cn).

Yubei He is with the School of Information Science and Engineering, Shandong University, Qingdao, Shandong 266237, China (e-mail: heyubei@126.com).

Yunfei Chen is with the Department of Engineering, University of Durham, DH1 3LE Durham, U.K. (e-mail: Yunfei.Chen@durham.ac.uk).

El-Hadi M. Aggoune is with the Sensor Networks and Cellular Systems Research Center, University of Tabuk, Tabuk 47315, Saudi Arabia (e-mail: hadi.aggoune@gmail.com).

Color versions of one or more figures in this article are available at <https://doi.org/10.1109/TWC.2023.3233961>.

Digital Object Identifier 10.1109/TWC.2023.3233961

GU locations, a number of stochastic UAV channel models were proposed [12], [13], [14], [15], [16], [17], [18], [19]. In [12], wideband stochastic channel models were proposed based on the time delay line (TDL) structure from the measurement data. Using explicit geometry relationships among transmitter (Tx), receiver (Rx), and scatterers, geometry based stochastic models (GBSMs) were modeled in the 3D space. In [13], [14], and [15], the authors used cylinder to describe the scatterers around the GUs. Statistical properties like temporal autocorrelation functions (ACFs) and spatial cross-correlation functions (CCFs) were derived using the geometric relationships. Authors in [16] and [17] utilized the ellipsoid model to describe the wideband properties of UAV-to-ground MIMO channels. Besides, to obtain the scenario- and altitude-related channel parameters, deterministic methods were used. In [20], ray tracing was used to evaluate the UAV-to-ground link coverage range in an urban scenario. In [21], a UAV-to-ground large-scale fading model supporting millimeter wave (mmWave) band was developed based on ray tracing simulation. These deterministic channel models are precise for site-specific scenarios but with limited pervasiveness.

As for the massive MIMO channel modeling, one of the most commonly considered channel properties is the near-field effect caused by the increasing size of antenna array. Under the near-field condition, the SWF and spatial non-stationary properties were verified by massive MIMO channel measurements in [22] and [23]. SWF means that multipath components (MPCs) departing from Tx, impinging at Rx, or interacting with scatterers within the Rayleigh distance will change the departure/arrival angles along the antenna array. Spatial non-stationarity means that different antenna elements may observe different cluster sets, i.e., clusters with birth and death along the antenna array. To incorporate the new characteristics of massive MIMO channels, a lot of channel models have been proposed using different modeling methods. For example, using correlation-based stochastic models (CBSMs), the MIMO channel response was determined by covariance matrix [24]. By introducing the survival matrix in the expression of covariance matrix, the CBSM was used to analyze the influence of birth-death process on massive MIMO channel capacity [25]. However, the covariance matrix cannot reflect the channel parameters at the cluster level. Thus, it cannot characterize SWF and non-stationary properties accurately. With more specific cluster level parameters, GBSMs can be used to model the SWF and spatial non-stationary properties. For instance, SWF effect and parameter drifting on the array axis were modeled through geometric relations in [26]. In [27], a non-stationary wideband GBSM was proposed based on the approximation of SWF using the second-order parabolic wavefront. A twin-cluster massive MIMO GBSM was proposed in [29]. By taking the non-stationarity in space, time, and frequency domains into account, this model can support massive MIMO channel simulation in multiple frequency bands and multiple scenarios. Furthermore, combining the characteristics of UAV channels and massive MIMO channels, GBSMs supporting SWF and non-stationary properties in both time and space domains were proposed in [30], [31], and [32]. Nevertheless, with the increase of array size, the complexity

of GBSMs mentioned above will increase proportionally, which makes system-level simulation, signal processing, and information theory investigation difficult.

To address the above issues, the beam domain channel model (BDCM) was proposed by transforming GBSM from the antenna domain into the beam domain using the unitary discrete Fourier transform (DFT) matrix [33]. It makes use of the sparsity of massive MIMO channels to reduce model complexity. This method has been widely used in various transmission techniques. For example, based on the BDCM, the beam division multiple access (BDMA) scheme was proposed in [34], which can provide higher spectral efficiency by allowing BS to communicate with multiple users via different orthogonal beams [35]. However, current BDCMs are mostly based on the far-field assumption. To meet the condition of unitary transformation matrix formation, although a few GBSMs and correlation-based stochastic models (CBSMs) for massive MIMO channels have illustrated that near-field propagation properties have significant impact on statistical properties and system performance, current BDCMs do not consider these new properties of massive MIMO channels. To fill this gap, in this paper, a novel 3D UAV BDCM is proposed by taking the SWF and spatial non-stationary properties into account. To the best of the authors' knowledge, the proposed BDCM for UAV communication is the first BDCM that considers the SWF and non-stationary properties. The main contributions and novelties of this paper include:

- We propose a novel massive MIMO 3D UAV-to-ground BDCM considering SWF and spatial non-stationarity. The proposed BDCM is obtained from the transformation of the corresponding GBSM through designed block transformation matrix. Besides, we verify that the proposed BDCM and the corresponding GBSM are unitary equivalent and interchangeable in both near-field and far-field conditions.
- Statistical properties of the proposed BDCM are derived, including the space-time-frequency correlation function (STF-CF), root-mean-squared (RMS) Doppler spread, beam spread, channel matrix collinearity (CMC), channel capacity, etc. The influences of SWF and non-stationary properties on channel characteristics and system performance are thoroughly analyzed. Besides, unique channel properties in beam domain, such as stronger temporal correlation and smaller Doppler spread than those in antenna domain, are revealed through simulation.
- The proposed BDCM is evaluated in terms of accuracy, complexity, and pervasiveness. The results show that the proposed BDCM can represent the SWF and non-stationary properties accurately in beam domain and achieve lower simulation complexity than the corresponding GBSM. The transformation relationships between BDCMs/GBSMs under far-field and near-field assumptions are discussed in detail.

The remainder of this paper is organized as follows. In Section II, the improved GBSM considering far-field assumption based on sub-array separation is illustrated. In Section III, the corresponding BDCM supporting SWF and non-stationarity is presented. Statistical properties such

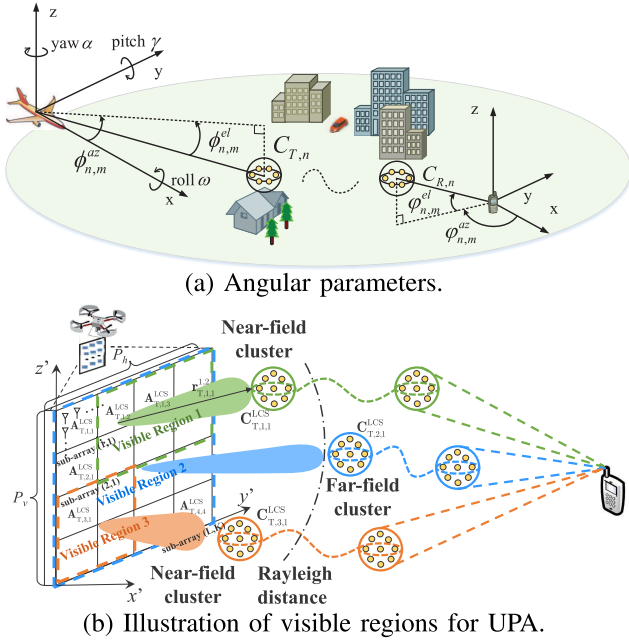


Fig. 1. The schematic plot of massive MIMO UAV communication channel.

as STF-CF, RMS beam/Doppler spread, and channel capacity are derived in Section IV. In Section V, simulation results are presented and analyzed. In Section VI, the performance of the proposed BDCM is evaluated. Finally, conclusions are drawn in Section VII.

Notation: Through the whole manuscript, $\|\cdot\|_F$ represents Frobenius norm, $\mathbb{E}\{\cdot\}$ accounts for statistical average, $\text{tr}(\cdot)$ represents trace operation, $(\cdot)^T$ denotes transpose operation, $(\cdot)^*$ denotes conjugate operation, $(\cdot)^H$ denotes conjugate transpose operation, \odot , \otimes , and $\langle \cdot, \cdot \rangle$ are the Schur-Hadamard (element-wise) product, Kronecker product, and inner product, respectively.

II. A NOVEL MASSIVE MIMO GBSM FOR UAV CHANNELS

Due to its flexible modeling process and good versatility in different scenarios, the GBSM is widely used in current standardized channel models, e.g., 3GPP 38.901 [36], WINNER+ [37], and METIS [38]. Hence, our proposed BDCM will be based on an equivalent GBSM. To facilitate understanding, the exposition of GBSM will start with a multiple-input single-output (MISO) configuration and then be extended to MIMO configuration.

Considering the UAV-to-ground channel between UAV and GU, the UAV equipped with a uniform planar array (UPA) containing P antenna elements is set as Tx, and the GU equipped with single antenna element is set as Rx. The GU can move in the horizontal plane with velocity vector \mathbf{v}_R and UAV can move in the 3D space with velocity vector \mathbf{v}_T . Besides, due to the airflow disturbances or mechanical vibration, the antenna array may experience the posture variation. In UAV systems, the posture variation is usually characterized by Euler angles, i.e., roll, pitch, and yaw angles (ω , γ , α) as shown in Fig. 1 (a). Without loss of generality, we consider a multi-bounce scattering propagation environment including

N clusters. Each cluster is characterized by a twin cluster structure containing first-bounce cluster $C_{T,n}$ and last-bounce cluster $C_{R,n}$. The propagation process between $C_{T,n}$ and $C_{R,n}$ is abstracted as a virtual link with the certain delay following the logarithmic distribution. The azimuth angles of departure (AAoDs), elevation angles of departure (EAoDs), azimuth angles of arrival (AAoAs), and elevation angles of arrival (EAoAs) of the m -th ray in n -th cluster are denoted by $\phi_{n,m}^{az}$, $\phi_{n,m}^{el}$, $\varphi_{n,m}^{az}$, and $\varphi_{n,m}^{el}$, respectively. Note that, similar to the current standardized channel modeling frameworks like 3GPP and WINNER, the parameterized description of clusters is used in the proposed GBSM. Related parameters and definitions are listed in Table I, and the corresponding stochastic distributions are included in Table II.

Specifically, the 3D locations of UAV, GU, and clusters are defined in the global coordinate system (GCS). The generated angular and distance parameters include the angular parameters $\phi_{n,m}^{az}$, $\phi_{n,m}^{el}$, $\varphi_{n,m}^{az}$, $\varphi_{n,m}^{el}$ that follow the normal distribution, and $D_{n,m}^T$, $D_{n,m}^R$ that follow the exponential distribution, as defined in Table I. Geometric relationships between Tx/Rx ($\mathbf{A}_T^{\text{GCS}}/\mathbf{A}_R^{\text{GCS}}$) and clusters ($\mathbf{C}_{T,n,m}^{\text{GCS}}/\mathbf{C}_{R,n,m}^{\text{GCS}}$) at the initial time instant t_0 are determined by

$$\begin{aligned} \mathbf{C}_{T,n,m}^{\text{GCS}}(t_0) &= \mathbf{A}_T^{\text{GCS}}(t_0) + D_{n,m}^T \cdot \begin{bmatrix} \cos \phi_{n,m}^{az} \cdot \cos \phi_{n,m}^{el} \\ \sin \phi_{n,m}^{az} \cdot \cos \phi_{n,m}^{el} \\ \sin \phi_{n,m}^{el} \end{bmatrix} \\ \mathbf{C}_{R,n,m}^{\text{GCS}}(t_0) &= \mathbf{A}_R^{\text{GCS}}(t_0) + D_{n,m}^R \cdot \begin{bmatrix} \cos \varphi_{n,m}^{az} \cdot \cos \varphi_{n,m}^{el} \\ \sin \varphi_{n,m}^{az} \cdot \cos \varphi_{n,m}^{el} \\ \sin \varphi_{n,m}^{el} \end{bmatrix}. \end{aligned} \quad (1)$$

At each time instant, the global coordinates $\mathbf{C}_{T,n,m}^{\text{GCS}}(t)$, $\mathbf{C}_{R,n,m}^{\text{GCS}}(t)$, $\mathbf{A}_T^{\text{GCS}}(t)$, and $\mathbf{A}_R^{\text{GCS}}$ are updated according to the corresponding velocity vectors, e.g., $\mathbf{A}_T^{\text{GCS}}(t) = \mathbf{A}_T^{\text{GCS}}(t - \Delta t) + \mathbf{v}_T \Delta t$, and so on. We introduce the variable $\delta_P(t, \Delta t)$ to describe the variation in the transmission environment from time t to $t + \Delta t$. It represents the sum of the distances traveled by the Tx and Rx from time t to $t + \Delta t$, i.e.,

$$\delta_P(t, \Delta t) = \|\mathbf{v}_T(t) \Delta t\|_F + \|\mathbf{v}_R(t) \Delta t\|_F. \quad (2)$$

Then, the probability that a cluster survives in this period can be represented by

$$P_s(t, \Delta t) = \exp\left[-\lambda_R \left(\frac{\delta_P(t, \Delta t)}{D_c}\right)\right] \quad (3)$$

where D_c is a scenario-dependent coefficient controlling the spatial correlation. Typical values of D_c can be chosen at the same order as the correlation distance. The mean value of the number of new clusters can be expressed as

$$\mathbb{E}[N_{\text{new}}(t + \Delta t)] = \frac{\lambda_G}{\lambda_R} (1 - P_s(t, \Delta t)). \quad (4)$$

Considering the angular parameter drifting and cluster birth-death phenomenon along the array axis, the large size UPA is divided into several small size UPA, as shown in Fig. 1 (b). Cluster angular parameters within each sub-array are assumed to be consistent, i.e., conforming to the PWF assumption. For convenience, the coordinate of l -th column

TABLE I
DEFINITION OF SIGNIFICANT CHANNEL MODEL PARAMETERS

Symbol	Definition
$\mathbf{C}_{T,n,m}^{\text{GCS}}(t)/\mathbf{C}_{R,n,m}^{\text{GCS}}(t)$	Coordinates of scattering points of m -th ray in the first/last bounce cluster in GCS
$\mathbf{C}_{T,n,m}^{\text{LCS}}(t)/\mathbf{C}_{R,n,m}^{\text{LCS}}(t)$	Coordinates of scattering points of m -th ray in the first/last bounce cluster in LCS
$\mathbf{A}_T^{\text{GCS}}(t)/\mathbf{A}_R^{\text{GCS}}(t)$	Coordinates of first Tx/Rx antenna elements in GCS
$\mathbf{v}_T/\mathbf{v}_R$	Velocity vectors of Tx/Rx in GCS
$\mathbf{A}_{T,l,k}^{\text{LCS}}(t)$	Coordinate of first Tx antenna element in sub-array (l, k) at time instant t in LCS
$D_{n,m}^T/D_{n,m}^R$	Distances between Tx/Rx and scattering points of m -th ray in the first/last bounce cluster
$\phi_{n,m}^{\text{az}}/\phi_{n,m}^{\text{el}}$	AAoD and EAoD of the m -th ray in the n -th first bounce cluster
$\varphi_{n,m}^{\text{az}}/\varphi_{n,m}^{\text{el}}$	AAoA and EAoA of the m -th ray in the n -th first bounce cluster
$\omega/\gamma/\alpha$	Roll/pitch/yaw angles representing the UAV posture variation
P_h/P_v	Number of Tx antenna element in each row/column
d_h/d_v	Azimuth/elevation antenna spacing
λ_C^h/λ_C^v	Rate parameters of the visible regions range in azimuth/elevation direction
$\Phi_{n,m}$	Random initial phase of m -th ray in the n -th cluster in $[0, 2\pi)$
$\tau_{n,m}$	Time delay of m -th ray in the n -th cluster
$\beta_{n,m}$	Amplitude of m -th ray in the n -th cluster
M_n	Rays number in the n -th cluster

TABLE II
GENERATION OF SIGNIFICANT CHANNEL MODEL PARAMETERS

Parameters	Distribution	Generation process
$\tau_{n,m}$	Exponential	Randomly generated according to delay spread and delay scalar [30]
$\beta_{n,m}$	Log-normal	Generated according to time delay and per-cluster shadowing [28]
$\phi_{n,m}^{\text{az}}, \phi_{n,m}^{\text{el}}, \varphi_{n,m}^{\text{az}}, \varphi_{n,m}^{\text{el}}$	Wrapped Gaussian	Randomly generated according to 3GPP TR 36.777 [9]
$D_{n,m}^T, D_{n,m}^R$	Exponential	Generated by fitting measurement data [28]
M_n	Poisson	Determined by assumption [30]

k -th row (l, k) sub-array is described as $\mathbf{A}_{T,l,k}^{\text{LCS}} = [0, (l-1)P_h d_h/L, (k-1)P_v d_v/K]^T$ in the local coordinate system (LCS) by using $\mathbf{A}_T^{\text{GCS}}(t)$ as the origin, the broadside of UPA as x-axis, the horizontal direction as y-axis, and the vertical direction as z-axis. Then, the scatterer coordinate in LCS can be obtained by

$$\mathbf{C}_{T,n,m}^{\text{LCS}}(t) = [\mathbf{C}_{T,n,m}^{\text{GCS}}(t) - \mathbf{A}_T^{\text{GCS}}(t)] \mathbf{R} \quad (5)$$

where \mathbf{R} is the UAV rotation factor matrix, and can be expressed as

$$\begin{aligned} \mathbf{R} &= \mathbf{R}_Z(\alpha)\mathbf{R}_Y(\gamma)\mathbf{R}_X(\omega) \\ &= \begin{bmatrix} \cos \alpha(t) & -\sin \alpha(t) & 0 \\ \sin \alpha(t) & \cos \alpha(t) & 0 \\ 0 & 0 & 1 \end{bmatrix} \begin{bmatrix} \cos \gamma(t) & 0 & \sin \gamma(t) \\ 0 & 1 & 0 \\ -\sin \gamma(t) & 0 & \cos \gamma(t) \end{bmatrix} \\ &\times \begin{bmatrix} 1 & 0 & 0 \\ 0 & \cos \omega(t) & -\sin \omega(t) \\ 0 & \sin \omega(t) & \cos \omega(t) \end{bmatrix}. \end{aligned} \quad (6)$$

Since the influences of UAV mechanical wobbling, wind gusts, and random turning, the Euler angles of UAV will show periodic and random variation. Here, the sum-of-sinusoid (SoS) method is utilized to model the random and continuous variation of Euler angles. Taking the time-variant roll angle as

an example, the value of $\omega(t)$ is assumed as

$$\omega(t) = \sum_{i=1}^I A_{\omega,i} \cos(2\pi\epsilon_{\omega,i}t + \theta_{\omega,i}) + \omega(t_0) \quad (7)$$

where $A_{\omega,i} \sim \mathcal{N}(\mu_{\omega,A}, \sigma_{\omega,A}^2)$, $\epsilon_{\omega,i} \sim \mathcal{N}(\mu_{\omega,\epsilon}, \sigma_{\omega,\epsilon}^2)$, and $\theta_{\omega,i} \sim \mathcal{U}(0, 2\pi)$ denote the amplitude, frequency, and initial phase of the i -th sinusoid ($i = 1, 2, \dots, I$), respectively. Similarly, the yaw angle and pitch angles can be modeled in the same way. For compactness, they are omitted here.

Due to the large size of antenna array aperture, clusters can be classified as far-field clusters \mathcal{C}_F and near-field clusters \mathcal{C}_N . The classification criteria is whether the distance between the cluster and antenna array is larger than the Rayleigh distance, $d = 2L_a^2/\lambda$, where L_a denotes antenna array aperture and λ is the wavelength. For example, let us assume a carrier frequency of $f_c = 11$ GHz, which is a medium priority frequency band for future wireless communication systems [38], [39], and numbers of antenna elements in each row/column is $P_h = P_v = 32$, the array aperture can be calculated as $L_a = \frac{32\sqrt{2}c}{f_c} = 1.23$ m, and the Rayleigh distance can be calculated as $d_R = \frac{2L_a^2 f_c}{c} = 111.6$ m, which means that, with given parameter setting, scattering clusters within 111.6 m will be seen as near-field clusters. Note that in the proposed model, LoS and non-LoS (NLoS) components are modeled similarly. If the distance between the Tx and Rx is smaller than the

Rayleigh distance, the LoS path will be regarded as near-field path and included in \mathcal{C}_N . Otherwise, it will be regarded as far-field path and included in \mathcal{C}_F . The far-field clusters have constant parameters including power, AAoD, EAoD, etc., for each sub-array. On the contrary, the parameters of near-field clusters will show variations for different sub-arrays, e.g., AAoD and EAoD drifting caused by the change of relative positions, and cluster birth-death process for different antenna pairs. Thus, the channel transfer function (CTF) of the UPA MISO channel in the antenna domain can be expressed as

$$\mathbf{H}(t, f) = \mathbf{H}^F(t, f) + \mathbf{H}^N(t, f) \quad (8)$$

where $\mathbf{H}^F(t, f)$ and $\mathbf{H}^N(t, f)$ are CTF matrices of far-field and near-field components, which can be expressed as

$$\mathbf{H}^F(t, f) = \sum_{n \in \mathcal{C}_F} \sum_{m=1}^{M_n} \beta_{n,m} e^{j[2\pi(\int_{t_0}^t \nu_{n,m}(t)dt - f\tau_{n,m}) + \Phi_{n,m}]} \cdot \mathbf{U}(\theta_{n,m}^{az}, \theta_{n,m}^{el}) \quad (9)$$

$$\mathbf{H}^N(t, f) = \sum_{n \in \mathcal{C}_N} \sum_{m=1}^{M_n} \beta_{n,m} e^{j[2\pi(\int_{t_0}^t \nu_{n,m}(t)dt - f\tau_{n,m}) + \Phi_{n,m}]} \cdot \tilde{\mathbf{U}}(\theta_{n,m}^{az}, \theta_{n,m}^{el}) \quad (10)$$

with $\Phi_{n,m}$ being the random initial phase of m -th ray in n -th cluster, $\nu_{n,m}$ being the time-variant Doppler frequency as

$$\nu_{n,m}(t) = \frac{\langle \mathbf{C}_{T,n,m}^{\text{GCS}} - \mathbf{A}_T^{\text{GCS}}, \mathbf{v}_T \rangle}{\lambda \|\mathbf{C}_{T,n,m}^{\text{GCS}} - \mathbf{A}_T^{\text{GCS}}\|_F} + \frac{\langle \mathbf{C}_{R,n,m}^{\text{GCS}} - \mathbf{A}_R^{\text{GCS}}, \mathbf{v}_R \rangle}{\lambda \|\mathbf{C}_{R,n,m}^{\text{GCS}} - \mathbf{A}_R^{\text{GCS}}\|_F}. \quad (11)$$

Besides, $\mathbf{U}(\theta_{n,m}^{az}, \theta_{n,m}^{el}) \in \mathbb{C}^{P_v \times P_h}$ is the far-field response matrix of UPA with P_v rows and P_h columns, and can be obtained as

$$\mathbf{U}(\theta_{n,m}^{az}, \theta_{n,m}^{el}) = \begin{bmatrix} 1 & \dots & e^{j2\pi(P_h-1)\theta_{n,m}^{az}} \\ e^{j2\pi\theta_{n,m}^{el}} & \dots & e^{j2\pi[\theta_{n,m}^{el} + (P_h-1)\theta_{n,m}^{az}]} \\ \vdots & \ddots & \vdots \\ e^{j2\pi(P_v-1)\theta_{n,m}^{el}} & \dots & e^{j2\pi[(P_v-1)\theta_{n,m}^{el} + (P_h-1)\theta_{n,m}^{az}]} \end{bmatrix}. \quad (12)$$

Here, $\theta_{n,m}^{el}$ and $\theta_{n,m}^{az}$ are spatial frequencies in azimuth direction (y-axis in LCS) and elevation direction (z-axis in LCS) associated with the m -th path in the n -th cluster. The spatial frequency is also known as spatial-Doppler frequency, which can be expressed as $\theta = \langle \Omega, \tilde{\Omega} \rangle$ [40]. Here, Ω is the angle unit vector of the arrival/departure waves and $\tilde{\Omega}$ is the orientation of the antenna array. Besides, $\tilde{\mathbf{U}}(\theta_{n,m}^{az}, \theta_{n,m}^{el}) \in \mathbb{C}^{P_v \times P_h}$ is the near-field response matrix of UPA, which can be expressed by the block matrix

$$\tilde{\mathbf{U}}(\theta_{n,m}^{az}, \theta_{n,m}^{el}) = \begin{bmatrix} \tilde{\mathbf{U}}^{(1,1)} & \dots & \tilde{\mathbf{U}}^{(L,1)} \\ \tilde{\mathbf{U}}^{(1,2)} & \dots & \tilde{\mathbf{U}}^{(L,2)} \\ \vdots & \ddots & \vdots \\ \tilde{\mathbf{U}}^{(1,K)} & \dots & \tilde{\mathbf{U}}^{(L,K)} \end{bmatrix} \quad (13)$$

where $\tilde{\mathbf{U}}^{(l,k)}$ ($l = 1 \dots L, k = 1 \dots K$) is the response matrix of the k -th row and l -th column sub-array. By separating the

whole UPA into several sub-arrays, the near-field clusters can be seen as far-field clusters to sub-arrays with constant parameters and PWF due to the smaller array aperture. Therefore, the response matrix can be written as (14), shown at the bottom of the next page. Here, $\Delta d_{n,m}^{l,k}$ denotes the propagation distance difference between sub-array (l, k) and sub-array $(1, 1)$, i.e., $\Delta d_{n,m}^{l,k} = d_{n,m}^{l,k} - d_{n,m}^{1,1}$. Besides, $\theta_{n,m}^{az,l,k}$ and $\theta_{n,m}^{el,l,k}$ denote the spatial frequencies in the azimuth and elevation directions of sub-array (l, k) associated with the m -th path in the n -th cluster, i.e.,

$$\begin{aligned} \theta_{n,m}^{az,l,k} &= [0 \quad d_h/\lambda \quad 0] \cdot \mathbf{r}_{n,m}^{l,k} \\ \theta_{n,m}^{el,l,k} &= [0 \quad 0 \quad d_v/\lambda] \cdot \mathbf{r}_{n,m}^{l,k} \end{aligned} \quad (15)$$

where $\mathbf{r}_{n,m}^{l,k}$ denotes the unit vector from sub-array (l, k) to $\mathbf{C}_{T,n,m}$ in LCS, i.e.,

$$\mathbf{r}_{n,m}^{l,k} = (\mathbf{C}_{T,n,m}^{\text{LCS}} - \mathbf{A}_{T,l,k}^{\text{LCS}}) / d_{n,m}^{l,k} \quad (16)$$

where $d_{n,m}^{l,k} = \|\mathbf{C}_{T,n,m}^{\text{LCS}} - \mathbf{A}_{T,l,k}^{\text{LCS}}\|_F$ is the distance between $\mathbf{C}_{T,n,m}$ and the first element of sub-array (l, k) via the m -th path. $\Lambda_{n,m}^{l,k}$ denotes the birth-death factor of sub-array (l, k) affected by array domain non-stationarity. The birth-death phenomenon, which is widely observed in the large-scale array channel measurements [41], [42], can be caused by array blockage and changing antenna response for drifting MPC directions. The value of the birth-death factor is 1 or 0, representing if the scatterer is or is not visible to the sub-array. The set of birth-death factors can be represented by

$$\Lambda_{n,m} = \Lambda_{n,m}^v \otimes (\Lambda_{n,m}^h)^T \quad (17)$$

in which $\Lambda_{n,m}^v$ and $\Lambda_{n,m}^h$ are the birth-death vectors characterizing the visible region of m -th path in n -th cluster

$$\Lambda_{n,m}^v = [\mathbf{O}_{I_{n,m}^{v,s}-1}, \mathbf{E}_{I_{n,m}^{v,e}-I_{n,m}^{v,s}+1}, \mathbf{O}_{\frac{P_v}{K}-I_{n,m}^{v,e}}] \quad (18)$$

$$\Lambda_{n,m}^h = [\mathbf{O}_{I_{n,m}^{h,s}-1}, \mathbf{E}_{I_{n,m}^{h,e}-I_{n,m}^{h,s}+1}, \mathbf{O}_{\frac{P_h}{L}-I_{n,m}^{h,e}}] \quad (19)$$

where \mathbf{O}_n and \mathbf{E}_n stand for the zero and one vectors with n entries, $I_{n,m}^{h/v,s}$ and $I_{n,m}^{h/v,e}$ are the start sub-array indexes and the end sub-array indexes, which are determined by the horizontal and vertical dimensions of the visible region as

$$\mathcal{I}_{n,m}^{h/v} = (I_{n,m}^{h/v,e} - I_{n,m}^{h/v,s}) \cdot d_{h/v}. \quad (20)$$

In general, the channel non-stationarity in the array domain is not isotropic. Specifically, the lengths of cluster visible region in horizontal and vertical directions are different, and can be modeled as independent random variables following an exponential distribution, i.e., $\mathcal{L}_{n,m}^{h/v} \sim \text{Exp}(\lambda_C^{h/v})$ [41], and mean values of visible regions range in azimuth and elevation directions are $1/\lambda_C^h$ and $1/\lambda_C^v$, respectively.

III. A NOVEL MASSIVE MIMO BDCM FOR UAV CHANNELS

Considering the multi-antenna equipped at both Tx and Rx sides, i.e., the massive MIMO configuration, the dimension of the UPA response matrix should be reduced to one to ensure the two-dimensional channel matrix structure. For ease

of analysis, $\mathbf{U}^{l,k}$ and $\tilde{\mathbf{U}}^{l,k}$ are replaced by $\text{vec}(\mathbf{U}^{l,k})$ and $\text{vec}(\tilde{\mathbf{U}}^{l,k})$ in (6)-(10). Besides, the response matrix at Rx side \mathbf{V} is also introduced and vectorized to one column $\text{vec}(\mathbf{V})$. The formation of \mathbf{V} is similar to \mathbf{U} . The channel matrices $\mathbf{H}^F(t, f)$ and $\mathbf{H}^N(t, f)$ are rearranged in the order of sub-array index as

$$\mathbf{H}^F(t, f) = \sum_{n \in \mathcal{C}_F} \sum_{m=1}^{M_n} \beta_{n,m} e^{j[2\pi(\int_{t_0}^t \nu_{n,m}(t)dt - f\tau_{n,m}) + \Phi_{n,m}]} \cdot [\text{vec}(\mathbf{V})] \cdot [\text{vec}(\mathbf{U}^{l,k})]_{l=1..L, k=1..K}^T \quad (21)$$

$$\mathbf{H}^N(t, f) = \sum_{n \in \mathcal{C}_N} \sum_{m=1}^{M_n} \beta_{n,m} e^{j[2\pi(\int_{t_0}^t \nu_{n,m}(t)dt - f\tau_{n,m}) + \Phi_{n,m}]} \cdot [\text{vec}(\mathbf{V})] \cdot [\text{vec}(\tilde{\mathbf{U}}^{l,k})]_{l=1..L, k=1..K}^T \quad (22)$$

where $[\text{vec}(\mathbf{U}^{l,k})]_{l=1..L, k=1..K}$ stands for the vector consisting of sub-array response vectors in the order of the sub-array index, and $\text{vec}(\mathbf{V})$ is the response vectors of Rx antenna array, which has the similar structure as $\text{vec}(\mathbf{U})$. In this study, we assume a common scenario that the UAV carrying aerial base station offers the wireless access for GUs. For this application, the aerial base station can be equipped with a massive MIMO antenna array (more than 64 antenna elements), and GU is usually equipped with traditional antenna array (4, 16, or similar numbers of antenna elements). Due to the limited array aperture at Rx, we assume that all clusters are far-field clusters for Rx.

Based on the proposed GBSM, the BDCM is generated through the DFT operation for different sub-arrays as

$$\begin{aligned} \mathbf{H}_B(t, f) &= \mathbf{V}_B^H (\mathbf{H}^F(t, f) + \mathbf{H}^N(t, f)) \tilde{\mathbf{U}}_B \\ &= \mathbf{H}_B^F(t, f) + \mathbf{H}_B^N(t, f) \end{aligned} \quad (23)$$

where \mathbf{V}_B is the transform matrix from antenna domain channel matrix to beam domain channel matrix at Rx. Under the far-field PWF assumption, $\mathbf{V}_B \in \mathbb{C}^{Q \times Q}$ can be written as

$$\mathbf{V}_B = \mathbf{V}_B^{el} \otimes \mathbf{V}_B^{az} \quad (24)$$

where

$$\begin{aligned} \mathbf{V}_B^{az} &= \frac{1}{\sqrt{Q_h}} [\mathbf{a}(\theta_i^{az})]_{i=1, \dots, Q_h} \in \mathbb{C}^{Q_h \times Q_h} \\ \mathbf{V}_B^{el} &= \frac{1}{\sqrt{Q_v}} [\mathbf{b}(\theta_j^{el})]_{j=1, \dots, Q_v} \in \mathbb{C}^{Q_v \times Q_v}. \end{aligned} \quad (25)$$

The columns of \mathbf{V}_B^{az} and \mathbf{V}_B^{el} are response vectors associated with Q_h and Q_v uniformly spaced spatial frequencies, i.e.,

$$\mathbf{a}(\theta_i^{az}) = \left[1, e^{j2\pi\theta_i^{az}}, \dots, e^{j2\pi(Q_h-1)\theta_i^{az}} \right]$$

$$\mathbf{b}(\theta_j^{el}) = \left[1, e^{j2\pi\theta_j^{el}}, \dots, e^{j2\pi(Q_v-1)\theta_j^{el}} \right]. \quad (26)$$

Here, $\theta_i^{az} = \frac{i}{Q_h} - 0.5$ and $\theta_j^{el} = \frac{j}{Q_v} - 0.5$ are the assigned azimuth and elevation spatial frequencies of whole Rx array. Under the half wavelength antenna spacing configuration, the values of θ_i^{az} and θ_j^{el} are in $[-0.5, 0.5]$.

Considering the SWF and near-field assumptions, the transform matrix $\tilde{\mathbf{U}}_B$ is a block matrix, i.e., $\tilde{\mathbf{U}}_B = \text{blockdiag}(\tilde{\mathbf{U}}_B^{l,k})_{l=1..L, k=1..K}$, in which $\tilde{\mathbf{U}}_B^{l,k}$ is the beam-forming matrix for the (l, k) sub-array as

$$\tilde{\mathbf{U}}_B^{l,k} = \tilde{\mathbf{U}}_B^{el,k} \otimes \tilde{\mathbf{U}}_B^{az,l} \quad (27)$$

where

$$\begin{aligned} \tilde{\mathbf{U}}_B^{az,l} &= \frac{1}{\sqrt{P_h/L}} [\tilde{\mathbf{a}}(\tilde{\theta}_{i'}^{az,l})]_{i'=1, \dots, \frac{P_h}{L}} \in \mathbb{C}^{\frac{P_h}{L} \times \frac{P_h}{L}} \\ \tilde{\mathbf{U}}_B^{el,k} &= \frac{1}{\sqrt{P_v/K}} [\tilde{\mathbf{b}}(\tilde{\theta}_{j'}^{el,k})]_{j'=1, \dots, \frac{P_v}{K}} \in \mathbb{C}^{\frac{P_v}{K} \times \frac{P_v}{K}} \end{aligned} \quad (28)$$

The columns of $\tilde{\mathbf{U}}_B^{az,l}$ and $\tilde{\mathbf{U}}_B^{el,k}$ are response vectors associated with P_h/L and P_v/K uniformly spaced spatial frequencies, i.e.,

$$\begin{aligned} \tilde{\mathbf{a}}(\tilde{\theta}_{i'}^{az}) &= \left[1, e^{j2\pi\tilde{\theta}_{i'}^{az}}, \dots, e^{j2\pi(\frac{P_h}{L}-1)\tilde{\theta}_{i'}^{az}} \right] \\ \tilde{\mathbf{b}}(\tilde{\theta}_{j'}^{el}) &= \left[1, e^{j2\pi\tilde{\theta}_{j'}^{el}}, \dots, e^{j2\pi(\frac{P_v}{K}-1)\tilde{\theta}_{j'}^{el}} \right]. \end{aligned} \quad (29)$$

Here, $\theta_{i'}^{az,l} = \frac{(i'-1)L+l}{P_h} - 0.5$ and $\theta_{j'}^{el,k} = \frac{(j'-1)K+k}{P_v} - 0.5$ are the assigned azimuth and elevation spatial frequencies of the sub-array (l, k) in $[-0.5, 0.5]$.

To illustrate the transformation clearly, Fig. 2 shows the generation process of the proposed BDCM matrix \mathbf{H}_B from corresponding GBSM matrix \mathbf{H} , where the Tx array is divided into 4 sub-arrays, i.e., $L = K = 2$. Besides, $\mathbf{H}^{(l,k)}$ denotes the GBSM channel matrix for sub-array (l, k) .

Through the transformation of the antenna domain channel matrix $\mathbf{H}(t, f)$ into the beam domain channel matrix $\mathbf{H}_B(t, f) = \mathbf{H}_B^F(t, f) + \mathbf{H}_B^N(t, f)$, the BDCM can represent the coupling of different beams between Tx and Rx. Utilizing the nature of Kronecker product and equality $(\mathbf{A} \otimes \mathbf{B})(\mathbf{C} \otimes \mathbf{D}) = (\mathbf{AC}) \otimes (\mathbf{BD})$, the elements in $\mathbf{H}_B^F(t, f)$ and $\mathbf{H}_B^N(t, f)$ can be derived as

$$\begin{aligned} [\mathbf{H}_B^F]_{q,p} &= [\mathbf{V}_B^H]_{q,:} \cdot \mathbf{H}^F[\tilde{\mathbf{U}}_B^*]_{:,p} \\ &= \sum_{n \in \mathcal{C}_F} \sum_{m=1}^{M_n} \beta_{n,m} e^{j[2\pi(\int_{t_0}^t \nu_{n,m}(t)dt - f\tau_{n,m}) + \Phi_{n,m}]} \\ &\quad \cdot e^{j2\pi \left[\frac{(l-1)\theta_{n,m}^{el} P_h}{L} + \frac{(k-1)\theta_{n,m}^{az} P_v}{K} \right]} \end{aligned}$$

$$\tilde{\mathbf{U}}^{(l,k)} = \Lambda_{n,m}^{l,k} \cdot e^{j\frac{2\pi}{\lambda}(\Delta d_{n,m}^{l,k})} \begin{bmatrix} 1 & \dots & e^{j2\pi(\frac{P_h}{L}-1)\theta_{n,m}^{az,l,k}} \\ e^{j2\pi\theta_{n,m}^{el,l,k}} & \dots & e^{j2\pi[\theta_{n,m}^{el,l,k} + (\frac{P_h}{L}-1)\theta_{n,m}^{az,l,k}]} \\ \vdots & \ddots & \vdots \\ e^{j2\pi(\frac{P_v}{K}-1)\theta_{n,m}^{el,l,k}} & \dots & e^{j2\pi[(\frac{P_v}{K}-1)\theta_{n,m}^{el,l,k} + (\frac{P_h}{L}-1)\theta_{n,m}^{az,l,k}]} \end{bmatrix}. \quad (14)$$

$$\begin{aligned}
 \tilde{\mathbf{U}}_B^{l,k} &= \tilde{\mathbf{U}}_B^{el,k} \in \mathbb{C}^{Q_v \times Q_v} \otimes \tilde{\mathbf{U}}_B^{az,l} \in \mathbb{C}^{Q_h \times Q_h} & \left(\frac{P}{4} \times \frac{P}{4}\right) \cdots \\
 \mathbf{V}_B &= \mathbf{V}_B^{el} \in \mathbb{C}^{P_v \times P_v} \otimes \mathbf{V}_B^{az} \in \mathbb{C}^{P_h \times P_h} \\
 \mathbf{V}_B^H &\times \left[\mathbf{H}^{(1,1)} \quad \mathbf{H}^{(1,2)} \quad \mathbf{H}^{(2,1)} \quad \mathbf{H}^{(2,2)} \right] \times \tilde{\mathbf{U}}_B & \tilde{\mathbf{U}}_B \in \mathbb{C}^{P_v \times P_h} \\
 \mathbf{V}_B &\in \mathbb{C}^{Q \times Q} & \mathbf{H} \in \mathbb{C}^{Q \times P}
 \end{aligned}$$

Fig. 2. The proposed BDCM matrix \mathbf{H}_B from corresponding GBSM matrix \mathbf{H} , i.e., $\mathbf{H}_B(t, f) = \mathbf{V}_B^H \mathbf{H}(t, f) \tilde{\mathbf{U}}_B$, where the Tx array is divided into 4 sub-arrays.

$$\begin{aligned}
 & \cdot \left[\tilde{\mathbf{a}}(\vartheta_{i'}^{az,l})^H \otimes \tilde{\mathbf{b}}(\vartheta_{j'}^{el,k})^H \right] \cdot \left[\tilde{\mathbf{a}}(\vartheta_{n,m}^{az}) \otimes \tilde{\mathbf{b}}(\vartheta_{n,m}^{el}) \right] \\
 & \cdot \left[\mathbf{a}(\theta_i^{az})^H \otimes \mathbf{b}(\theta_j^{el})^H \right] \cdot \left[\mathbf{a}(\theta_{n,m}^{az}) \otimes \mathbf{b}(\theta_{n,m}^{el}) \right] \\
 = & \sum_{n \in \mathcal{C}_F} \sum_{m=1}^{M_n} \beta_{n,m} e^{j \left[2\pi \left(\int_{t_0}^t \nu_{n,m}(t) dt - f \tau_{n,m} \right) + \Phi_{n,m} \right]} \\
 & \cdot e^{j 2\pi \left[\frac{(l-1)\theta_{n,m}^{el} P_h}{L} + \frac{(k-1)\theta_{n,m}^{az} P_v}{K} \right]} \\
 & \cdot f \left(\frac{P_h}{L}; \tilde{\vartheta}_{i'}^{az,l} - \vartheta_{n,m}^{az} \right) \cdot f \left(\frac{P_v}{K}; \tilde{\vartheta}_{j'}^{el,k} - \vartheta_{n,m}^{el} \right) \\
 & \cdot f(Q_h; \theta_i^{az} - \theta_{n,m}^{az}) \cdot f(Q_v; \theta_j^{el} - \theta_{n,m}^{el}) \quad (30)
 \end{aligned}$$

$$\begin{aligned}
 & [\mathbf{H}_B^N]_{q,p} \\
 = & [\mathbf{V}_B^H]_{q,:} \mathbf{H}^N [\tilde{\mathbf{U}}_B^*]_{:,p} \\
 = & \sum_{n \in \mathcal{C}_N} \sum_{m=1}^{M_n} \Lambda_{n,m}^{l,k} \beta_{n,m} \\
 & \times e^{j \left[2\pi \left(\int_{t_0}^t \nu_{n,m}(t) dt - f \tau_{n,m} + \frac{\Delta a_{n,m}^{l,k}}{\lambda} \right) + \Phi_{n,m} \right]} \\
 & \cdot \left[\tilde{\mathbf{a}}(\vartheta_{i'}^{az,l})^H \otimes \tilde{\mathbf{b}}(\vartheta_{j'}^{el,l})^H \right] \cdot \left[\tilde{\mathbf{a}}(\vartheta_{n,m}^{az,l,k}) \otimes \tilde{\mathbf{b}}(\vartheta_{n,m}^{el,l,k}) \right] \\
 & \cdot \left[\mathbf{a}(\theta_i^{az})^H \otimes \mathbf{b}(\theta_j^{el})^H \right] \cdot \left[\mathbf{a}(\theta_{n,m}^{az}) \otimes \mathbf{b}(\theta_{n,m}^{el}) \right] \\
 = & \sum_{n \in \mathcal{C}_N} \sum_{m=1}^{M_n} \Lambda_{n,m}^{l,k} \beta_{n,m} \\
 & \times e^{j \left[2\pi \left(\int_{t_0}^t \nu_{n,m}(t) dt - f \tau_{n,m} + \frac{\Delta a_{n,m}^{l,k}}{\lambda} \right) + \Phi_{n,m} \right]} \\
 & \cdot f \left(\frac{P_h}{L}; \tilde{\vartheta}_{i'}^{az,l} - \tilde{\vartheta}_{n,m}^{az,l,k} \right) \cdot f \left(\frac{P_v}{K}; \tilde{\vartheta}_{j'}^{el,k} - \tilde{\vartheta}_{n,m}^{el,l,k} \right) \\
 & \cdot f(Q_h; \theta_i^{az} - \theta_{n,m}^{az}) \cdot f(Q_v; \theta_j^{el} - \theta_{n,m}^{el}) \quad (31)
 \end{aligned}$$

Here, the index p represents the 3D beam at Tx, i.e., $p = \frac{P_h P_v}{LK} [L \cdot (k-l) + l - 1] + \frac{P_h}{L} \cdot (j-1) + i'$, l and k are sub-array indexes in azimuth and vertical directions, i' and j' are beam indexes of the sub-array (l, k) in azimuth and vertical directions. The index q represents the 3D beam at Rx. According to the beam assignment, $q = Q_v \cdot (j-1) + i$, i and j are beam indexes in azimuth and vertical directions, respectively. The function $f(N; x)$ is defined as

$$f(N; x) = e^{j\pi x(N-1)} \frac{\sin(\pi x N)}{N \sin(\pi x)} \quad (32)$$

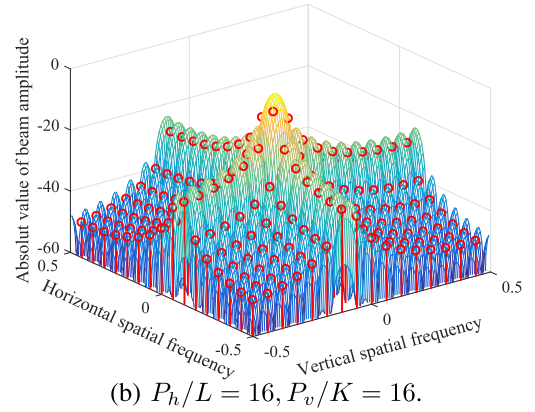
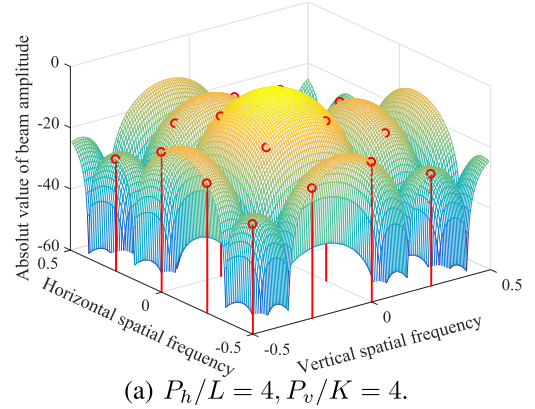


Fig. 3. Beam assignment and beam response amplitude in dB for different sub-array sizes.

When the dimensions of the array are large enough, the function $f(N; x)$ can be approximately represented by delta function according to the L'Hospital's rule, i.e., $f(N; x) \approx e^{j\pi x(N-1)}$, if $x = 0$, and $f(N; x) \approx 0$, if $x \neq 0$. Due to the sparsity of massive MIMO channels, the beam domain channel matrix \mathbf{H}_B is sparse. By only calculating the non-zero values in channel matrix and ignoring the zero values, the channel simulation complexity can be significantly reduced. To avoid confusion, part of symbols are defined in Table III.

The beam assignment and beam response amplitude for different sub-array sizes are presented in Fig. 3. The red stem line denotes the assignment of beam in spatial frequency, and the height of red stem line denotes the absolute amplitude of the corresponding beam derived from $f(N; x)$ using (30) and (31). The colored parametric surface in Fig. 3 represents the spatial frequency response of the sub-array obtained from the transformation of GBSM, i.e., matrix multiplication as shown in (23). The matching between derivation result and matrix operation result verifies the correctness of both derivation and operation. It also can be observed that the increasing of the sub-array size will lead to narrower beam pattern.

IV. STATISTICAL PROPERTIES

Given that the channel propagation is a stochastic process, the statistical properties are widely employed to analyze the channel properties and evaluate channel models. Some typical

TABLE III
DEFINITION OF SIGNIFICANT SYMBOLS

Symbol	Definition
$\mathbf{H}^F(t, f)/\mathbf{H}^N(t, f)$	Channel response matrix of far-field/near-field clusters in antenna domain from GBSM
$\mathbf{H}_B^F(t, f)/\mathbf{H}_B^N(t, f)$	Channel response matrix of far-field/near-field clusters in beam domain from BDCM
$\mathbf{U}/\tilde{\mathbf{U}}$	Steering vectors of Tx antenna array of far-field/near-field clusters
$\mathbf{U}^{l,k}/\tilde{\mathbf{U}}^{l,k}$	Steering vectors of Tx sub-array (l, k) of far-field/near-field clusters
\mathbf{V}	Steering vectors of Rx antenna array
$\tilde{\mathbf{U}}_B$	Transform matrix for Tx (far-field assumption)
\mathbf{V}_B	Transform matrix for Rx (near-field assumption)

channel statistical properties are quite different when the channel model is transformed from the antenna domain to the beam domain. In this section, we will calculate the statistical properties of the proposed BDCM.

A. STF-CF

For the proposed BDCM, the STF-CF is defined as the correlation between $[\mathbf{H}_{B,p,q}(t, f)]$ and $[\mathbf{H}_{B,p',q'}(t + \Delta t, f + \Delta f)]$, and can be calculated as

$$\begin{aligned} \gamma_{pq,p'q'}(\Delta t, \Delta f) \\ = \mathbb{E} \{ [\mathbf{H}_{B,p,q}(t, f)] [\mathbf{H}_{B,p',q'}(t + \Delta t, f + \Delta f)] \}. \end{aligned} \quad (33)$$

Since the channel matrix is transformed from the spatial domain to the beam domain in the proposed BDCM, the spatial cross correlation is represented by correlation between different beams. Considering the STF-CF at Tx side, according to (30), (33) can be further expressed as

$$\begin{aligned} \gamma_{pq,pq'}(\Delta t, \Delta f) \\ = \sum_{n=1}^N \sum_{m=1}^{M_n} \beta_{n,m}^2 \cdot \Lambda_{n,m}^{l,k} \\ \cdot e^{j2\pi(\Delta f \tau_{n,m} - \nu_{n,m} \Delta t)} \cdot e^{j\pi \frac{(P_h - 1)\Delta j}{P_h}} \cdot e^{j\pi \frac{(P_v - 1)\Delta i}{P_v}} \\ \cdot \frac{K^2 \sin\left(\pi(\theta_{n,m}^{el} - \tilde{\theta}_j^{el})\right) \sin\left(\pi(\theta_{n,m}^{el} - \tilde{\theta}_{j'}^{el})\right)}{P_v^2 \sin\left(\pi \frac{P_v}{K}(\theta_{n,m}^{el} - \tilde{\theta}_j^{el})\right) \sin\left(\pi \frac{P_v}{K}(\theta_{n,m}^{el} - \tilde{\theta}_{j'}^{el})\right)} \\ \cdot \frac{L^2 \sin\left(\pi(\theta_{n,m}^{az} - \tilde{\theta}_i^{az})\right) \sin\left(\pi(\theta_{n,m}^{az} - \tilde{\theta}_{i'}^{az})\right)}{P_h^2 \sin\left(\pi \frac{P_h}{K}(\theta_{n,m}^{az} - \tilde{\theta}_i^{az})\right) \sin\left(\pi \frac{P_h}{L}(\theta_{n,m}^{az} - \tilde{\theta}_{i'}^{az})\right)}. \end{aligned} \quad (34)$$

Since the beams in the same sub-array are concentrated in the same part of $\mathbf{H}_B(t, f)$, the beam correlation is used to characterize the correlation between different beams in the same sub-array. As for the correlation between different sub-arrays, it can be characterized by the channel matrix CMC which will be discussed in the next subsection.

B. CMC

The CMC is a measure of the change in the space structure of two matrices of the same size. It can compare the subspaces of two complex matrices and obtain their similarity. The CMC

between two sub-arrays (l, k) and (l', k') can be expressed as

$$a_{lk,l'k'} = \mathbb{E} \left\{ \frac{\text{tr}\{[\mathbf{H}_B]_{:,D(l,k)}[\mathbf{H}_B]_{D(l',k'),:}^H\}}{\|[\mathbf{H}_B]_{D(l,k),:}\|_F \|[\mathbf{H}_B]_{:,D(l',k')}\|_F} \right\} \quad (35)$$

where $[\mathbf{H}_B]_{:,D(l,k)}$ and $[\mathbf{H}_B]_{:,D(l',k')}$ denote beam domain channel matrices of sub-arrays (l, k) and (l', k') , $D(l, k)$ and $D(l', k')$ are the beam index set corresponding to sub-arrays (l, k) and (l', k') , e.g.,

$$\begin{aligned} D(l, k) = \left[\frac{P_h P_v}{LK} \cdot (L \cdot (k - 1) + l - 1) + 1 : \right. \\ \left. \frac{P_h P_v}{LK} \cdot (L \cdot (k - 1) + l) \right]. \end{aligned} \quad (36)$$

which contains all index numbers of sub-array (l, k) , i.e., totally $\frac{P_h P_v}{LK}$ index numbers from $\frac{P_h P_v}{LK} \cdot (L \cdot (k - 1) + l - 1) + 1$ to $\frac{P_h P_v}{LK} \cdot (L \cdot (k - 1) + l)$. The CMC takes values in the range of $(0, 1)$. When the CMC is 0, it means that the two sub-array beam channel matrices do not have any linear relationship and the sub-arrays are completely uncorrelated, i.e., the propagation environment of two sub-arrays are totally different. When the CMC is 1, it means that the sub-array beam channel matrices have a linear scaling relationship.

C. Doppler PSD

The movement of the Tx and Rx will lead to shift in the carrier frequency as Doppler frequency shift. Doppler PSD reflects the distribution of signal power at different Doppler frequencies, which can be obtained by calculating the Fourier transform of the temporal ACF as

$$S_n(\nu, t) = \int_{-\infty}^{\infty} r_n(t, \Delta t) e^{-j2\pi\nu\Delta t} d\Delta t \quad (37)$$

where ν is the Doppler frequency in Hz, and $r_n(t, \Delta t)$ is the temporal ACF, which can be obtained by selecting the same beam index and making the frequency difference zero in the local STF-CF. Meanwhile, the RMS Doppler spread σ_ν measuring the dispersion of signal in Doppler frequency domain can be calculated as the second-order central moment of Doppler PSD [32].

D. Beam Spread

The beam spread describes the power dispersion of the beam domain channel over different beam directions. Similar

to the angular spread, the RMS azimuth beam spread can be defined as

$$\sigma_B^{az} = \sqrt{\frac{\sum_{p,q=1}^{P,Q} |[\mathbf{H}_B]_{p,q}|^2 (\tilde{\theta}_i^{az} - \mu^{az})^2}{\sum_{p,q=1}^{P,Q} |[\mathbf{H}_B]_{p,q}|^2}} \quad (38)$$

where μ^{az} is the mean value of azimuth angle $\tilde{\theta}_i^{az}$ and can be calculated as the ratio of summation of the power-weighted azimuth angles to the total channel power, i.e.,

$$\mu^{az} = \frac{\sum_{p,q=1}^{P,Q} |[\mathbf{H}_B]_{p,q}|^2 \tilde{\theta}_i^{az}}{\sum_{p,q=1}^{P,Q} |[\mathbf{H}_B]_{p,q}|^2}. \quad (39)$$

E. Channel Capacity

Channel capacity is an important metric of the communication system performance. Assuming that the CSI is only known at the Rx side, the single-user channel capacity can be calculated as

$$C = \mathbb{E} \left\{ \log_2 \det \left(\mathbf{I} + \frac{SNR}{P} \bar{\mathbf{H}} \bar{\mathbf{H}}^H \right) \right\} \quad (40)$$

where SNR denotes the signal to noise ratio (SNR), $\bar{\mathbf{H}}$ is the normalized channel matrix, which can be obtained by

$$\bar{\mathbf{H}} = \mathbf{H} \cdot \left\{ \frac{1}{PQ} \|\mathbf{H}\|_F \right\}^{-\frac{1}{2}}. \quad (41)$$

For GBSM or BDCM, $\mathbf{H} = \mathbf{H}(t, f)$ or $\mathbf{H} = \mathbf{H}_B(t, f)$ are substituted into (41), respectively.

F. Stationary Time Interval

Due to the agile maneuverability of the UAV, the UAV-to-ground channel shows more degrees of freedom in 3D space, making it difficult for beam tracking and mapping. In this section, the stationary time interval, which is defined as the maximum duration within which the channel can be seen as stationary, is used to quantitatively determine the degree of channel changing. Here, we use the CMC to measure the correlation coefficient between two beam domain channel matrices [43]. Then the stationary time interval is obtained as the largest time duration within which the correlation coefficient beyond the certain threshold c_{thresh} , i.e.,

$$T_s(t) = \max \left\{ \Delta t \mid \frac{\text{tr} \{ \mathbf{H}_B(t, f) \mathbf{H}_B^H(t + \Delta t, f) \}}{\|\mathbf{H}_B(t, f)\|_F \|\mathbf{H}_B^H(t + \Delta t, f)\|_F} \geq c_{\text{thresh}} \right\}. \quad (42)$$

The correlation coefficient threshold is empirically set to 90%. This value can be adjusted according to the specific requirements.

V. RESULTS AND DISCUSSIONS

In order to study the massive MIMO UAV-to-ground channel characteristics in beam domain and reveal how PWF and spatial non-stationarity affect the UAV massive MIMO channels, we will present results of STF-CF, CMC, beam spread, and channel capacity using the proposed novel BDCM

and corresponding GBSM. The definitions and calculations of statistical properties of the GBSM are can be find in [32], so we do not repeat them here. Unless otherwise specified, the following parameters are chosen in the simulation: $P = 4096$, $P_h = P_v = 64$, and $f_c = 11$ GHz. At the initial time, the UAV height is set to 50 m, the location of GU is set to 50 m from UAV horizontally, so the initial link distance is 70 m. The parameters of MPCs such as powers, delays, and angles are generated according to 3GPP TR 36.777 in the urban macro cell. The following parameters are chosen in the simulation: delay spread in dB $DS = -7.65$, angular spread parameters in dB including azimuth angle spread of arrival $ASA = 1.79$, azimuth angle spread of departure $ASD = -1.32$, elevation angle spread of arrival $ESA = 1.17$, elevation angle spread of departure $ESD = -1.15$, mean value of UAV-cluster distance $1/\lambda_d^T = 80$ m, velocity of UAV $v_T = 3$ m/s, and velocity of GU $v_R = 0$ m/s. The UPA at UAV side is separated in to $L \times K = 16$ sub-arrays, and $L = K = 4$. For the sake of simplicity, non-stationary assumption is abbreviated as NS.

Fig. 4 presents the amplitude distributions of beam domain channel elements. Fig. 4 (a) and Fig. 4 (b) compare the beam amplitude for same sub-array size but different sub-array indices. We can find that, due to the SWF and cluster birth-death mechanism, cluster number and parameters change for different sub-arrays. Fig. 4 (a) and Fig. 4 (c) present the beam amplitude with the same sub-array index but different sub-array sizes. We can observe that increment of the sub-array size will lead to more sparse channel matrix in the beam domain. The reason is that a larger sub-array size gives a smaller beam width, resulting in more zero values in the beam domain channel matrix. Fig. 4 (d) provides the beam matrix at Rx side for comparison. Since the angular spread parameters at the Rx side, i.e., ASA and ESA , are larger than those at the Tx side, i.e., ASD and ESD , the beam matrix at the Rx side is more intensive than that at the Tx side. Besides, Figs. 4 (e)~(g) are beam amplitude for whole UPA, i.e., combining beam amplitude matrices of different sub-arrays according to spatial frequencies. It can be observed that through division of the whole UPA, the MPCs in beam domain become more dispersive when spatial non-stationarity and SWF are introduced. This is because of the cluster birth-death effect caused by non-stationarity and cluster drifting in beam domain along the sub-array caused by SWF effect. At last, the whole beam matrix at 28 GHz band is provided in Fig. 4 (h) for comparison. Under the same half wavelength antenna spacing configuration, due to the smaller size of antenna array, the near-field effect becomes less obvious at 28 GHz than that at 11 GHz.

Fig. 5 provides simulation results of spatial CCF, i.e., the beam correlation in the sub-array. The rate parameters of visible regions range are set as $\lambda_C^h = 1.8$ and $\lambda_C^v = 1.1$. We can find that the beam correlation function in the azimuth domain has a smaller correlation coefficient. The reason for this is due to different cluster visible regions ranges for the azimuth and vertical directions. The smaller rate parameter in azimuth domain means each cluster can cover more sub-arrays, leading to larger beam correlation. Besides, simulation results with WSS assumption are provided for comparison.

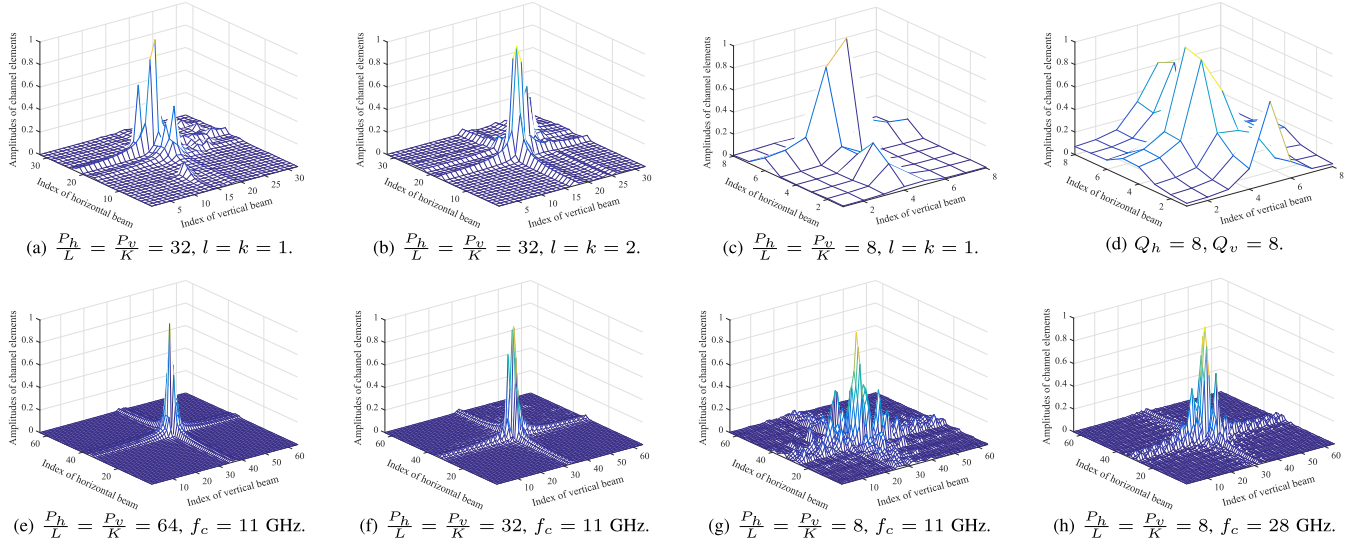


Fig. 4. Amplitude distributions of beam domain channel elements: (a)-(c) Tx side beam matrices of sub-arrays with different sizes and indexes, (d) Rx side beam matrix for comparison, (e)-(h) Tx side beam matrices of the whole array with different sub-array sizes and carrier frequencies.

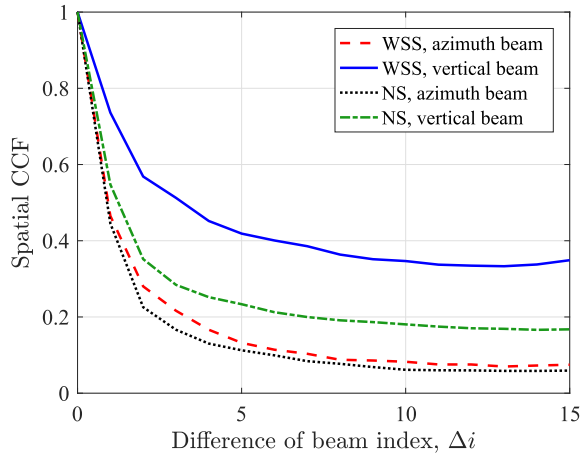


Fig. 5. The beam correlation in azimuth and elevation directions with WSS PWF and non-stationary SWF assumptions ($L = K = 2, P_h = P_v = 64, f_c = 11$ GHz, $d_h = d_v = \lambda/2, \alpha = 4/\pi, \gamma = 0$).

It can be observed that non-stationarity will decrease the beam correlation in both azimuth and elevation domains.

Fig. 6 and Fig. 7 compare the temporal ACFs and RMS Doppler spreads of proposed BDCM and equivalent GBSM. The consistency between the simulation model and simulation result of temporal ACF ensures the correctness of our simulations and derivations. Note that the simulation result is from the correlation operation of channel matrix obtained from (23), and the simulation model is computed according to (33). Using the same parameter setting, BDCM tends to have larger absolute value of ACF, which means that channel variation becomes slower when the GBSM is transformed to BDCM. Meanwhile, the RMS Doppler spread of BDCM is smaller than that of GBSM. The reason is that each element in BDCM only contains part of clusters within the beam direction range. Thus the multipath effect is suppressed in this case.

Fig. 8 compares CMC for different sub-arrays with different UAV-cluster distance settings. The distances between

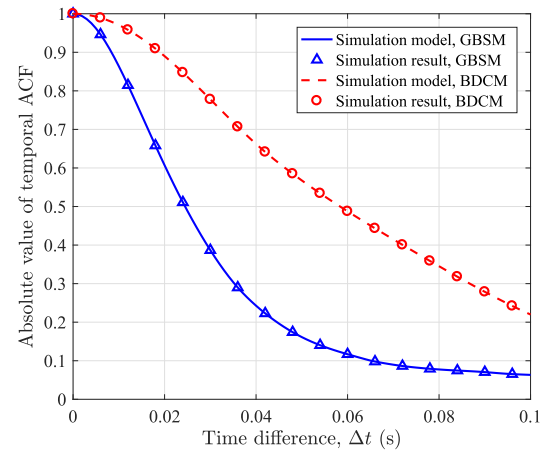


Fig. 6. Temporal ACFs of GBSM and BDCM ($L = K = 4, P_h = P_v = 64, f_c = 11$ GHz, $d_h = d_v = \lambda/2, v_T = 3$ m/s, $v_R = 0$ m/s, $\alpha = 4/\pi, \gamma = 0$).

transceiver and clusters are assumed to follow the exponential distribution. When the mean value of UAV-cluster distance $1/\lambda_d^T$ decreases from 160 m to 40 m, the CMC between different sub-arrays gradually decreases, illustrating the influence of SWF effect in the given simulation condition. The reason is that the number of near-field clusters will increase when the UAV-cluster distance $1/\lambda_d^T$ decreases, and the SWF property will lead to parameter drifting for all near-field clusters.

Fig. 9 shows the ergodic channel capacities of GBSM and BDCM under SWF non-stationary and PWF WSS assumptions. It can be found that the channel capacities of GBSM and BDCM are the same due to the equivalence between the BDCM and corresponding GBSM. Furthermore, when the massive MIMO configuration is used, SWF and non-stationary properties will produce considerable gain in channel capacity. However, with the smaller size MIMO configuration, SWF and non-stationary properties have insignificant influence on the capacity.

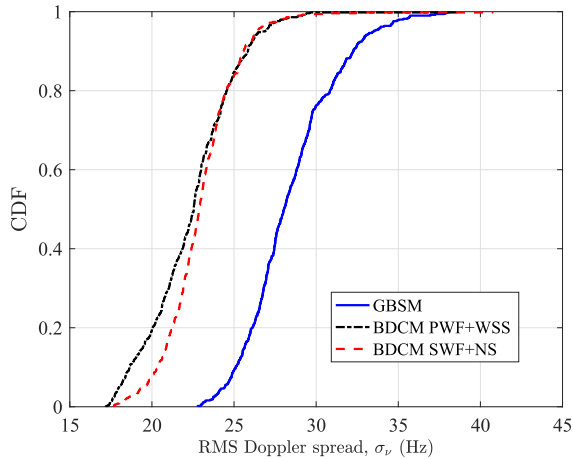


Fig. 7. Doppler spreads of GBSM with single antenna pair and BDCM with different propagation assumptions ($L = K = 4, P_h = P_v = 64, f_c = 11$ GHz, $d_h = d_v = \lambda/2, v_T = 3$ m/s, $v_R = 0$ m/s, $\alpha = 4/\pi, \gamma = 0$).

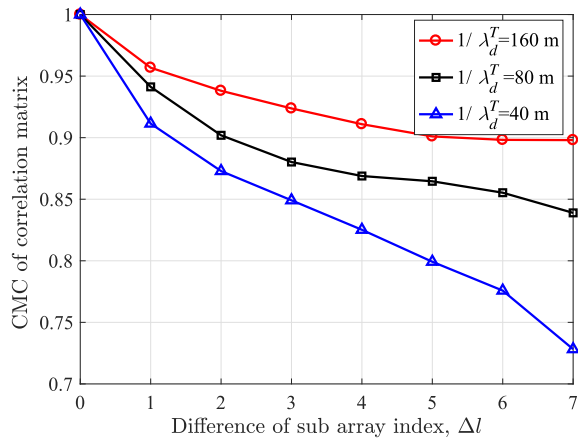


Fig. 8. The CMC between sub-arrays with different UAV-cluster distances ($L = K = 8, P_h = P_v = 64, f_c = 11$ GHz, $d_h = d_v = \lambda/2, \alpha = 4/\pi, \gamma = 0$).

Fig. 10 presents the cumulative distribution function (CDF) of stationary time interval of the proposed BDCM. Through the simulation we found that the UAV vibration tends to have impact on the channel non-stationarity. The stationary time interval becomes shorter when vibration amplitude and frequency become larger. Besides, the stationary interval is also affected by the UAV velocity. The fast movement of UAV will decrease the stationary interval significantly.

VI. CHANNEL MODEL EVALUATION

Three indicators are often used to evaluate the performances of channel models, i.e., accuracy, complexity, and pervasiveness. In this section, we will evaluate the proposed BDCM and equivalent GBSM, and compare the performances of them.

A. Accuracy

The accuracy of channel models reflects the capability of channel model mimicking the propagation environment. The commonly used method of accuracy evaluation is comparing

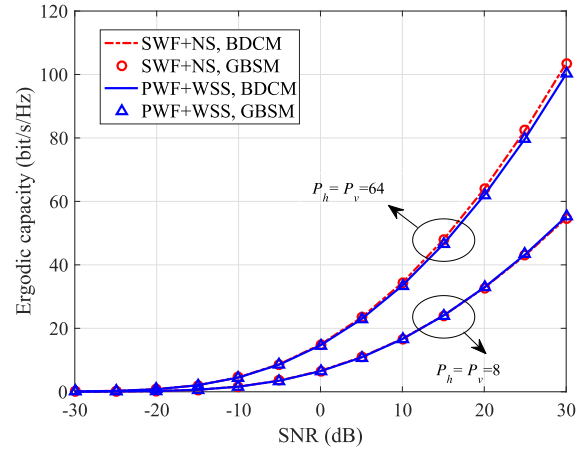


Fig. 9. Channel capacities of GBSM and BDCM with different propagation assumptions and antenna configurations ($L = K = 4, Q_h = Q_v = 2, f_c = 11$ GHz, $d_h = d_v = \lambda/2, \alpha = 4/\pi, \gamma = 0$).

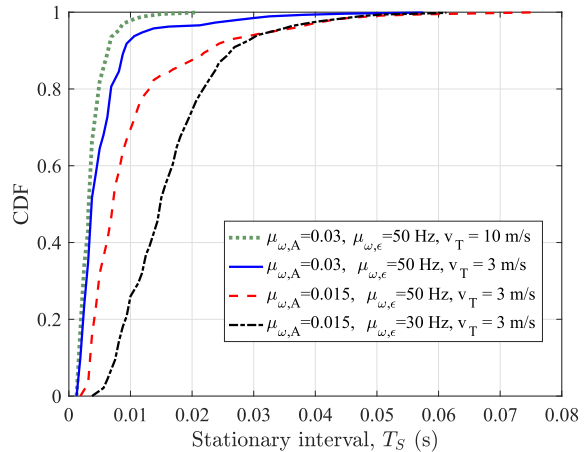


Fig. 10. Stationary time interval of BDCM with different jittering parameters ($L = K = 4, P_h = P_v = 64, f_c = 11$ GHz, $d_h = d_v = \lambda/2, \alpha = 4/\pi, \gamma = 0$).

the statistical properties of channel model with those from channel measurement data. Since beam domain is physically related to angular domain, i.e., in the proposed BDCM, beams are separated according to angle exactly, and MPCs are mapped into beam and angular domains simultaneously, we use the angular measurement results to validate the proposed model. Fig. 11 shows the azimuth beam spread of the proposed BDCM and measurement angular spread in [44]. The measurement was conducted at 3.5 GHz in a UAV-to-cellular scenario, and the angular spread was estimated according to identified MPCs. The simulation parameters are chosen as $f_c = 3.5$ GHz, $ESA = 1.47$, and $\lambda_C^v = 1.9$. The simulated beam spread fits the measurement angular spread well, which demonstrates that the proposed BDCM can represent realistic channel propagation in angular domain accurately. Besides, the comparison between PWF and SWF shows that the SWF property will lead to a larger beam spread.

B. Complexity

The channel model complexity represents the computational operations needed for channel coefficient generation. Here, the computational complexities of proposed BDCM and GBSM

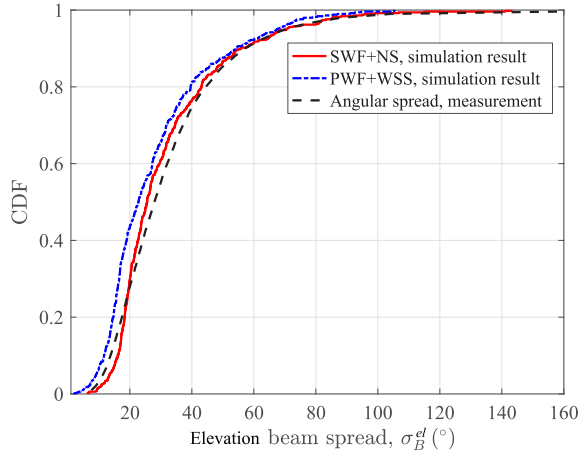


Fig. 11. Simulation results of beam spread with different propagation assumptions and measurement results [44] ($L = 2, K = 1, P_h = 8, P_v = 4, f_c = 3.5$ GHz, $ESA = 1.47, \lambda_C^v = 1.9, d_h = d_v = \lambda/2, \alpha = 4/\pi, \gamma = 0$).

are compared in terms of the number of “real operations (ROs)” [45]. The number of ROs of any mathematical operations is calculated based on four basic operations, namely real addition, real multiplication, real division, and table lookup, with each operation requiring one RO. Since in each time instant the channel generation process is the same, we only analyze the number of ROs needed for one time instant, and the RO number for the whole simulation process is proportional to the number of ROs needed for one time instant.

1) *The Complexity of the Equivalent GBSM*: The required number of ROs for generating the proposed GBSM can be calculated as

$$C_G = N(t)M_n PQC_{G,A} + LKC_{G,S} \quad (43)$$

where $C_{G,A}$ is the required RO number for response of each ray and single antenna pair, and $C_{G,S}$ is the required RO number for parameter generation of each ray and each sub-array. According to (21) and (22), the operations needed for single antenna includes 4 multiplication operations (4 ROs), 1 add operation (1 RO), 1 exponential operation (15 ROs), and 1 assignment operation (1 RO), i.e., $C_{G,A} = 4 + 1 + 15 + 1 = 21$. As for the operations needed for parameter generation of each sub-array, it includes 1 coordinate vector subtraction (3 ROs), 1 modular operation (6 ROs), 4 coordinate dot multiplication (12 ROs), and 2 multiplication operations (2 ROs), i.e., $C_{G,S} = 3 + 6 + 12 + 2 = 23$.

2) *The Complexity of the Proposed BDCM*: The required number of ROs for generating the proposed BDCM can be calculated as

$$C_B = N(t)M_n LKC_{B,S} \quad (44)$$

where $C_{B,s}$ is the required RO number for parameter generation of each ray and each sub-array. Utilizing the sparse property of BDCM, we only need to calculate the channel coefficient with non-zero value, which can greatly reduce the calculation complexity. According to (30)-(32), the operations needed for single MPC includes 1 vector subtraction operations (6 ROs), 1 modular operation (6 ROs), 4 coordinate dot

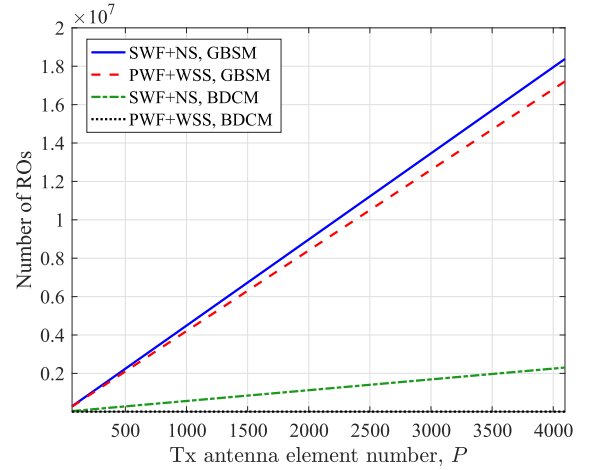


Fig. 12. The complexity of BDCM and equivalent GBSM with different propagation assumptions (SWF+NS: $P_h/L = P_v/K = 8$, PWF + WSS: $L = K = 1$).

multiplication (12 ROs), 2 mapping operation (match the MPC spatial frequency to the closest beam, 8 ROs), 1 exponent operation (15 ROs), and 1 assignment operation (1 RO), i.e., $C_{B,S} = 3 + 6 + 12 + 8 + 15 + 1 = 45$. The complexity of the proposed BDCM and corresponding GBSM with Tx antenna number from 64 to 4096 is shown in Fig. 12. The evaluation results show that the complexity of the proposed BDCM is far less than that of GBSM, especially with the increase of antenna number.

C. Pervasiveness

Pervasiveness reflects the compatibility and flexibility of channel model for different scenarios, frequencies, system configurations, and applications. The proposed BDCM is based on the parameterized modeling framework and has uniform parameter set with GBSM, which is widely used in mainstream standard channel models. Thus, the proposed BDCM can be adapted to diverse standard scenarios and configurations. Specifically, using different simulation parameter settings in 3GPP TR36.777 [9], the proposed BDCM is applicable for urban macro cell scenario, urban mini cell scenario, etc. By adjusting antenna parameters, the proposed BDCM can flexibly support both conventional antenna array ($L = K = 1$) and massive antenna array ($L \in (1, P_h), K \in (1, P_v)$) at both Tx and Rx.

Furthermore, the proposed BDCM can be transformed to equivalent GBSM using the transformation matrix $\tilde{\mathbf{U}}_B^*/\tilde{\mathbf{V}}_B^*$, and the inverse transformation also holds using the conjugate transpose matrix $\tilde{\mathbf{U}}_B^T/\tilde{\mathbf{V}}_B^T$ due to the conjugation of the transformation matrix. The proof of the conjugation of transpose matrix is given in the Appendix. For clarity, the transformation and simplification relations of proposed GBSM and BDCM are shown in Fig. 13. It is worth mentioning that by setting sub-array size to 1, both proposed GBSM and BDCM turn to SWF non-stationary GBSM in antenna element level, i.e., the non-stationary channel model in [30], which calculates the phase according to propagation distance corresponding to different antenna elements respectively. By setting the sub-array

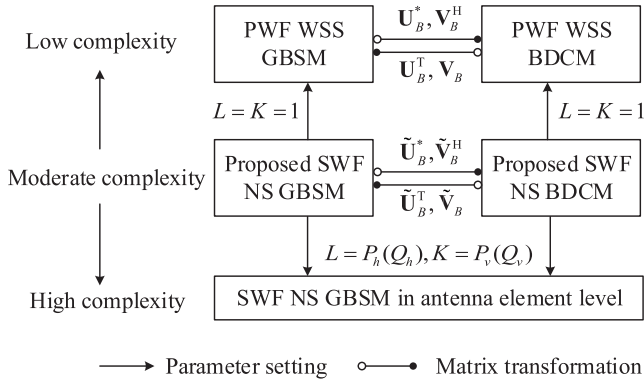


Fig. 13. Transformation and simplification relations of proposed GBSM/BDCM, and other models with different wavefront and non-stationary assumptions.

number to 1, i.e., $L = K = 1$, SWF and non-stationary conditions will reduce to PWF and WSS conditions, and the proposed BDCM will turn to the traditional BDCM with lower complexity.

VII. CONCLUSION

In this paper, we have proposed a 3D BDCM for massive MIMO UAV-to-ground communications. By introducing SWF and spatial non-stationary properties, the proposed BDCM can characterize the near-field effect over the large UPA antenna configuration. Based on the proposed model, the statistical properties such as the STF-CF, RMS Doppler spread, beam spread, CMC, and channel capacity, have been derived and simulated. We have found that the near-field propagation condition will decrease the correlation between different sub-arrays, and increase the whole channel capacity. Furthermore, while considering the mobile scenario for UAV communications, the BDCM shows lower time variability and is more insensitive to the Doppler effect compared with equivalent GBSM. Finally, the performance of the proposed BDCM has been evaluated in terms of accuracy, complexity, and pervasiveness. The evaluation results have shown that proposed BDCM has high accuracy as well as low complexity. Through the matrix operation and parameter setting, the proposed BDCM can be adapted to near-field/far-field scenarios as well as converted to WSS and non-stationary GBSMs, indicating flexibility of the proposed BDCM.

APPENDIX

According to the matrix form in (27), the proof of the conjugation of $(\tilde{\mathbf{U}}_B^{l,k})^*$ is as follows

$$(\tilde{\mathbf{U}}_B^{l,k})^T (\tilde{\mathbf{U}}_B^{l,k})^* = (\tilde{\mathbf{U}}_B^{el,k} \otimes \tilde{\mathbf{U}}_B^{az,l})^T (\tilde{\mathbf{U}}_B^{el,k} \otimes \tilde{\mathbf{U}}_B^{az,l})^* \quad (45)$$

Utilizing the nature of Kronecker product and equality $(\mathbf{A} \otimes \mathbf{B})(\mathbf{C} \otimes \mathbf{D}) = (\mathbf{AC}) \otimes (\mathbf{BD})$, (45) can be further calculated as

$$\begin{aligned} & (\tilde{\mathbf{U}}_B^{el,k} \otimes \tilde{\mathbf{U}}_B^{az,l})^T (\tilde{\mathbf{U}}_B^{el,k} \otimes \tilde{\mathbf{U}}_B^{az,l})^* \\ &= \left[(\tilde{\mathbf{U}}_B^{el,k})^T (\tilde{\mathbf{U}}_B^{el,k})^* \right] \otimes \left[(\tilde{\mathbf{U}}_B^{az,l})^T (\tilde{\mathbf{U}}_B^{az,l})^* \right]. \quad (46) \end{aligned}$$

Considering an element in the first item of (46), we have

$$\begin{aligned} & \left[(\tilde{\mathbf{U}}_B^{el,k})^T (\tilde{\mathbf{U}}_B^{el,k})^* \right]_{p_1, p_2} \\ &= (\tilde{\mathbf{U}}_B^{el,k})_{:, p_1}^T (\tilde{\mathbf{U}}_B^{el,k})_{:, p_2}^* \\ &= \frac{1}{P_v/K} \cdot \tilde{\mathbf{b}} (\tilde{\theta}_{p_1}^{az,l})^T \tilde{\mathbf{b}} (\tilde{\theta}_{p_2}^{az,l})^* \\ &= \frac{1}{P_v/K} \cdot \sum_{s=1}^{P_v/K} e^{j2\pi(s-1)(\tilde{\theta}_{p_1}^{az} - \tilde{\theta}_{p_2}^{az})} \\ &= \frac{1}{P_v/K} \cdot \frac{1 - e^{j2\pi(\tilde{\theta}_{p_1}^{az} - \tilde{\theta}_{p_2}^{az})} P_v/K}{1 - e^{j2\pi(\tilde{\theta}_{p_1}^{az} - \tilde{\theta}_{p_2}^{az})}}. \quad (47) \end{aligned}$$

According to the L'Hospital's rule, in (47) we can find that

$$\left[(\tilde{\mathbf{U}}_B^{el,k})^T (\tilde{\mathbf{U}}_B^{el,k})^* \right]_{p_1, p_2} = \begin{cases} 1, & \text{if } p_1 = p_2 \\ 0, & \text{if } p_1 \neq p_2. \end{cases} \quad (48)$$

Therefore, $(\tilde{\mathbf{U}}_B^{el,k})^T (\tilde{\mathbf{U}}_B^{el,k})^*$ is an identity matrix, and $(\tilde{\mathbf{U}}_B^{el,k})^*$ is a unitary matrix. Similarly, $(\tilde{\mathbf{U}}_B^{az,k})^T (\tilde{\mathbf{U}}_B^{az,k})^*$ can be proved to be an identity matrix. Utilizing the nature of Kronecker product in (46), it also can be proved that $(\tilde{\mathbf{U}}_B^{l,k})^*$ is a unitary matrix. Then, the whole transformation block matrix $\tilde{\mathbf{U}}_B^* = \text{blockdiag}(\tilde{\mathbf{U}}_B^{l,k})_{l=1 \dots L, k=1 \dots K}^*$ is also a unitary matrix since that

$$\begin{aligned} \tilde{\mathbf{U}}_B^T \tilde{\mathbf{U}}_B^* &= \text{blockdiag} \left[(\tilde{\mathbf{U}}_B^{l,k})^T (\tilde{\mathbf{U}}_B^{l,k})^* \right]_{l=1 \dots L, k=1 \dots K} \\ &= \mathbf{I}. \quad (49) \end{aligned}$$

REFERENCES

- [1] Y. Zeng, Q. Wu, and R. Zhang, "Accessing from the sky: A tutorial on UAV communications for 5G and beyond," *Proc. IEEE*, vol. 107, no. 12, pp. 2327–2375, Mar. 2019.
- [2] Z. Zhang et al., "6G wireless networks: Vision, requirements, architecture, and key technologies," *IEEE Veh. Technol. Mag.*, vol. 14, no. 3, pp. 28–41, Sep. 2019.
- [3] HUAWEI. 6G: *The Next Horizon White Paper*. Accessed: Jan. 15, 2022. [Online] <https://www.huawei.com/en/technology-insights/future-technologies/6g-white-paper>
- [4] C. X. Wang, J. Huang, H. Wang, X. Gao, X. You, and Y. Hao, "6G wireless channel measurements and models: Trends and challenges," *IEEE Veh. Technol. Mag.*, vol. 15, no. 4, pp. 22–32, Dec. 2020.
- [5] X.-H. You et al., "Towards 6G wireless communication networks: Vision, enabling technologies, and new paradigm shifts," *Sci. China Inf. Sci.*, vol. 64, no. 1, pp. 1–74, Jan. 2021, doi: 10.1007/s11432-020-2955-6.
- [6] Y. Zeng, R. Zhang, and T. J. Lim, "Wireless communications with unmanned aerial vehicles: Opportunities and challenges," *IEEE Commun. Mag.*, vol. 54, no. 5, pp. 36–42, May 2016.
- [7] S. Hayat, E. Yanmaz, and R. Muzaffar, "Survey on unmanned aerial vehicle networks for civil applications: A communications viewpoint," *IEEE Commun. Surveys Tuts.*, vol. 18, no. 4, pp. 2624–2661, 4th Quart., 2016.
- [8] Y. Huang, Q. Wu, R. Lu, X. Peng, and R. Zhang, "Massive MIMO for cellular-connected UAV: Challenges and promising solutions," *IEEE Commun. Mag.*, vol. 59, no. 2, pp. 84–90, Feb. 2021.
- [9] *Study on Enhanced LTE Support for Aerial Vehicles (Release 15)*, document TR 36.777, v15.0.0, 3GPP, Dec. 2017.
- [10] C.-X. Wang, J. Bian, J. Sun, W. Zhang, and M. Zhang, "A survey of 5G channel measurements and models," *IEEE Commun. Surveys Tuts.*, vol. 20, no. 4, pp. 3142–3168, 4th Quart., 2018.
- [11] A. A. Khuwaja, Y. Chen, N. Zhao, M.-S. Alouini, and P. Dobbins, "A survey of channel modeling for UAV communications," *IEEE Commun. Surveys Tuts.*, vol. 20, no. 4, pp. 2804–2821, 4th Quart., 2018.

- [12] R. Sun and D. W. Matolak, "Air-ground channel characterization for unmanned aircraft systems Part II: Hilly and mountainous settings," *IEEE Trans. Veh. Technol.*, vol. 66, no. 3, pp. 1913–1925, Mar. 2017.
- [13] L. Zeng, X. Cheng, C.-X. Wang, and X. Yin, "A 3D geometry-based stochastic channel model for UAV-MIMO channels," in *Proc. IEEE Wireless Commun. Netw. Conf. (WCNC)*, San Francisco, CA, USA, Mar. 2017, pp. 1–5.
- [14] Y. Li and X. Cheng, "New deterministic and statistical simulation models for non-isotropic UAV-MIMO channels," in *Proc. 9th Int. Conf. Wireless Commun. Signal Process. (WCSP)*, Nanjing, China, Oct. 2017, pp. 1–6.
- [15] L. Zeng, X. Cheng, C.-X. Wang, and X. Yin, "Second order statistics of non-isotropic UAV Ricean fading channels," in *Proc. IEEE 86th Veh. Technol. Conf. (VTC-Fall)*, Toronto, ON, Canada, Sep. 2017, pp. 1–5.
- [16] H. Chang, J. Bian, C.-X. Wang, Z. Bai, W. Zhou, and E.-H. M. Aggoune, "A 3D non-stationary wideband GBSM for low-altitude UAV-to-ground V2V MIMO channels," *IEEE Access*, vol. 7, pp. 70719–70732, 2019.
- [17] H. Jiang, Z. Zhang, and G. Gui, "Three-dimensional non-stationary wideband geometry-based UAV channel model for A2G communication environments," *IEEE Access*, vol. 7, pp. 26116–26122, 2019.
- [18] Z. Ma, B. Ai, R. He, Z. Zhong, and M. Yang, "A non-stationary geometry-based MIMO channel model for millimeter-wave UAV networks," *IEEE J. Sel. Areas Commun.*, vol. 39, no. 10, pp. 2960–2974, Oct. 2021.
- [19] Z. Ma et al., "Impact of UAV rotation on MIMO channel characterization for air-to-ground communication systems," *IEEE Trans. Veh. Technol.*, vol. 69, no. 11, pp. 12418–12431, Nov. 2020.
- [20] Q. Feng, J. McGeehan, E. K. Tameh, and A. R. Nix, "Path loss models for air-to-ground radio channels in urban environments," in *Proc. VTC, Melbourne, VIC, Australia*, Jun. 2006, pp. 2901–2905.
- [21] W. Khawaja, O. Ozdemir, and I. Guvenc, "UAV Air-to-Ground channel characterization for mmWave systems," in *Proc. IEEE 86th Veh. Technol. Conf. (VTC-Fall)*, Toronto, ON, Canada, Sep. 2017, pp. 1–5.
- [22] S. Payami and F. Tufvesson, "Channel measurements and analysis for very large array systems at 2.6 GHz," in *Proc. IEEE EUCAP*, Prague, Czech Republic, Mar. 2012, pp. 433–437.
- [23] A. Bernland, M. Gustafsson, C. Gustafson, and F. Tufvesson, "Estimation of spherical wave coefficients from 3-D positioner channel measurements," *IEEE Antennas Wireless Propag. Lett.*, vol. 11, pp. 608–611, 2012.
- [24] W. Weichselberger, M. Herdin, H. Ozelcik, and E. Bonek, "A stochastic MIMO channel model with joint correlation of both link ends," *IEEE Trans. Wireless Commun.*, vol. 5, no. 1, pp. 90–100, Jan. 2006.
- [25] S. Wu, C.-X. Wang, E.-H.-M. Aggoune, and M. M. Alwakeel, "A novel kronecker-based stochastic model for massive MIMO channels," in *Proc. IEEE/CIC Int. Conf. Commun. China (ICCC)*, Shenzhen, China, Nov. 2015, pp. 1–6.
- [26] Y. Chen, Y. Li, S. Sun, X. Cheng, and X. Chen, "A twin-multi-ring channel model for massive MIMO system," in *Proc. 16th Int. Symp. Commun. Inf. Technol. (ISCIT)*, Qingdao, China, Sep. 2016, pp. 606–610.
- [27] C. F. Lopez and C.-X. Wang, "Novel 3-D non-stationary wideband models for massive MIMO channels," *IEEE Trans. Wireless Commun.*, vol. 17, no. 5, pp. 2893–2905, May 2018.
- [28] X. Cai et al., "An empirical air-to-ground channel model based on passive measurements in LTE," *IEEE Trans. Veh. Technol.*, vol. 68, no. 2, pp. 1140–1154, Feb. 2019.
- [29] J. Bian, C.-X. Wang, X. Gao, X. You, and M. Zhang, "A general 3D non-stationary wireless channel model for 5G and beyond," *IEEE Trans. Wireless Commun.*, vol. 20, no. 5, pp. 3211–3224, May 2021.
- [30] H. Chang et al., "A novel non-stationary 6G UAV-to-ground wireless channel model with 3D arbitrary trajectory changes," *IEEE Int. Things J.*, vol. 8, no. 12, pp. 9865–9877, Jun. 2021.
- [31] Y. Liu, C.-X. Wang, H. Chang, Y. He, and J. Bian, "A novel non-stationary 6G UAV channel model for maritime communications," *IEEE J. Sel. Areas Commun.*, vol. 39, no. 10, pp. 2992–3005, Oct. 2021.
- [32] C.-X. Wang, Z. Lv, X. Gao, X. You, Y. Hao, and H. Haas, "Pervasive wireless channel modeling theory and applications to 6G GBSMs for all frequency bands and all scenarios," *IEEE Trans. Veh. Technol.*, vol. 71, no. 9, pp. 9159–9173, Sep. 2022.
- [33] C. Sun, X. Q. Gao, S. Jin, M. Matthaiou, Z. Ding, and C. Xiao, "Beam division multiple access transmission for massive MIMO communications," *IEEE Trans. Commun.*, vol. 63, no. 6, pp. 2170–2184, Jun. 2015.
- [34] C. Sun, X. Gao, S. Jin, M. Matthaiou, Z. Ding, and C. Xiao, "Beam division multiple access for massive MIMO downlink transmission," in *Proc. IEEE Int. Conf. Commun. (ICC)*, London, U.K., Jun. 2015, pp. 1–6.
- [35] L. You, X. Gao, G. Y. Li, X.-G. Xia, and N. Ma, "BDMA for millimeter-wave/terahertz massive MIMO transmission with per-beam synchronization," *IEEE J. Sel. Areas Commun.*, vol. 35, no. 7, pp. 1550–1563, Jul. 2017.
- [36] *Study on Channel Model for Frequencies From 0.5 to 100 GHz (Release 14)*, document TR 38.901, v14.0.0, 3GPP, Mar. 2017.
- [37] J. Meinila et al., "WINNER+ final channel models," Wireless World Initiative New Radio (WINNER), Tech. Rep. CELTIC/CP5-026 D5.3, Jun. 2010.
- [38] V. Nurmela, "METIS channel models," Mobile Wireless Commun. Enablers Twenty-Two Inf. Soc. (METIS), ICT-317669/D1.4, Tech. Rep. D1.4 ICT-317669-METIS/D1.4, Jul. 2015.
- [39] M. Kim, Y. Konishi, Y. Chang, and J.-I. Takada, "Large scale parameters and double-directional characterization of indoor wideband radio multipath channels at 11 GHz," *IEEE Trans. Antennas Propag.*, vol. 62, no. 1, pp. 430–441, Jan. 2014.
- [40] B. H. Fleury, "First- and second-order characterization of direction dispersion and space selectivity in the radio channel," *IEEE Trans. Inf. Theory*, vol. 46, no. 6, pp. 2027–2044, Sep. 2000.
- [41] J. Li et al., "On 3D cluster-based channel modeling for large-scale array communications," *IEEE Trans. Wireless Commun.*, vol. 18, no. 10, pp. 4902–4914, Oct. 2019.
- [42] J. Huang, C.-X. Wang, R. Feng, J. Sun, W. Zhang, and Y. Yang, "Multi-frequency mmWave massive MIMO channel measurements and characterization for 5G wireless communication systems," *IEEE J. Sel. Areas Commun.*, vol. 35, no. 7, pp. 1591–1605, Jul. 2017.
- [43] M. Herdin, N. Czink, H. Ozelcik, and E. Bonek, "Correlation matrix distance, a meaningful measure for evaluation of non-stationary MIMO channels," in *Proc. IEEE 61st Veh. Technol. Conf.*, Stockholm, Sweden, May 2005, pp. 136–140.
- [44] Y. Wang, R. Zhang, B. Li, X. Tang, and D. Wang, "Angular spread analysis and modeling of UAV air-to-ground channels at 3.5 GHz," in *Proc. 11th Int. Conf. Wireless Commun. Signal Process. (WCSP)*, Xi'an, China, Oct. 2019, pp. 1–5.
- [45] Y. Zhang, A. Ghazal, C.-X. Wang, H. Zhou, W. Duan, and E.-H.-M. Aggoune, "Accuracy-complexity tradeoff analysis and complexity reduction methods for non-stationary IMT—A MIMO channel models," *IEEE Access*, vol. 7, pp. 178047–178062, 2019.



Hengtai Chang (Member, IEEE) received the B.Sc. and Ph.D. degrees from the School of Information Science and Engineering, Shandong University, China, in 2016 and 2021, respectively. He is currently a Post-Doctoral Research Associate with the Purple Mountain Laboratories, China, and a Post-Doctoral Research Associate with the China National Mobile Communications Research Laboratory, Southeast University, China. His current research interests include UAV communications, wireless propagation channel measurements and channel modeling, and B5G/6G wireless communications.



Cheng-Xiang Wang (Fellow, IEEE) received the B.Sc. and M.Eng. degrees in communication and information systems from Shandong University, China, in 1997 and 2000, respectively, and the Ph.D. degree in wireless communications from Aalborg University, Denmark, in 2004.

He was a Research Assistant at the Hamburg University of Technology, Hamburg, Germany, from 2000 to 2001, a Visiting Researcher at Siemens AG Mobile Phones, Munich, Germany, in 2004, and a Research Fellow at the University of Agder, Grimstad, Norway, from 2001 to 2005. He has been with Heriot-Watt University, Edinburgh, U.K., since 2005, where he was promoted to a Professor, in 2011. In 2018, he joined as a Professor with Southeast University, Nanjing, China. He is also a part-time Professor with the Purple Mountain Laboratories, Nanjing. He has authored four books, three book chapters, and more than 480 papers in refereed journals and conference proceedings, including 27 highly cited papers. He has also delivered 24 invited keynote speeches/talks and 14 tutorials in international conferences. His current research interests include wireless channel measurements and modeling, 6G wireless communication networks, and electromagnetic information theory.

He is a member of the Academia Europaea (The Academy of Europe) and the European Academy of Sciences and Arts (EASA). He is a fellow of the Royal Society of Edinburgh (FRSE), IET, and the China Institute of Communications (CIC). He is an IEEE Communications Society Distinguished Lecturer in 2019 and 2020, a Highly-Cited Researcher recognized by Clarivate Analytics from 2017 to 2020, and one of the most cited Chinese Researchers recognized by Elsevier in 2021. He is currently an Executive Editorial Committee Member of the IEEE TRANSACTIONS ON WIRELESS COMMUNICATIONS. He has served as a TPC member, a TPC chair, and a general chair for more than 80 international conferences. He received 15 Best Paper Awards from IEEE GLOBECOM 2010, IEEE ICCT 2011, ITST 2012, IEEE VTC 2013Spring, IWCMC 2015, IWCMC 2016, IEEE/CIC ICC 2016, WPMC 2016, WOCC 2019, IWCMC 2020, WCSP 2020, CSPS2021, WCSP 2021, and IEEE/CIC ICC 2022. Also, he received the 2020-2022 "AI 2000 Most Influential Scholar Award Honourable Mention" in recognition of his outstanding and vibrant contributions in the field of the Internet of Things. He has served as an Editor for over ten international journals, including the IEEE TRANSACTIONS ON WIRELESS COMMUNICATIONS, from 2007 to 2009, the IEEE TRANSACTIONS ON VEHICULAR TECHNOLOGY, from 2011 to 2017, and the IEEE TRANSACTIONS ON COMMUNICATIONS, from 2015 to 2017. He was a Guest Editor (Lead Guest Editor) for Special Issue on Vehicular Communications and Networks of the IEEE JOURNAL ON SELECTED AREAS IN COMMUNICATIONS, Special Issue on Spectrum and Energy Efficient Design of Wireless Communication Networks, and Special Issue on Airborne Communication Networks. He was also a Guest Editor for Special Issue on Wireless Big Data of the IEEE TRANSACTIONS ON BIG DATA, and is a Guest Editor for Special Issue on Intelligent Resource Management for 5G and Beyond of the IEEE TRANSACTIONS ON COGNITIVE COMMUNICATIONS AND NETWORKING.



Ji Bian (Member, IEEE) received the B.Sc. degree in electronic information science and technology from Shandong Normal University, Jinan, China, in 2010, the M.Sc. degree in signal and information processing from the Nanjing University of Posts and Telecommunications, Nanjing, China, in 2013, and the Ph.D. degree in information and communication engineering from Shandong University, Jinan, in 2019. From 2017 to 2018, he was a Visiting Scholar at the School of Engineering and Physical Sciences, Heriot-Watt University, Edinburgh, U.K.

He is currently a Lecturer with the School of Information Science and Engineering, Shandong Normal University. His research interests include 6G channel modeling and wireless big data.



Rui Feng (Member, IEEE) received the B.Sc. degree in communication engineering and the M.Eng. degree in signal and information processing from Yantai University, China, in 2011 and 2014, respectively, and the Ph.D. degree in communication and information system from Shandong University, China, in 2018. From July 2018 to September 2020, she was a Lecturer at Ludong University, China. She is currently a Post-Doctoral Research Associate with the Purple Mountain Laboratories and Southeast University, China. Her research interests include

(ultra-) massive MIMO channel modeling theory and beam domain channel modeling.



Yubei He (Student Member, IEEE) received the B.Sc. degree from the School of Information Science and Engineering, Shandong University, Qingdao, China, in 2017, where she is currently pursuing the Ph.D. degree in information and communication engineering. Her current research interests include maritime communications, wireless propagation channel measurements and channel modeling, and B5G/6G wireless communications.



Yunfei Chen (Senior Member, IEEE) received the B.E. and M.E. degrees in electronics engineering from Shanghai Jiaotong University, Shanghai, China, in 1998 and 2001, respectively, and the Ph.D. degree from the University of Alberta in 2006. He is currently working as a Reader with the School of Engineering, The University of Warwick, U.K., and as a Professor with the Department of Engineering, Durham University, U.K. His research interests include wireless communications, performance analysis, joint radar communications designs, cognitive radios, wireless relaying, and energy harvesting.



El-Hadi M. Aggoune (Life Senior Member, IEEE) received the M.S. and Ph.D. degrees in electrical engineering from the University of Washington (UW), Seattle, WA, USA. He served at several universities in USA and abroad at many academic ranks, including the Endowed Chair Professor. He is listed as an Inventor in several patents, one of them assigned to the Boeing Company, USA. He is a Professional Engineer registered in the state of Washington. He is currently serving as a Professor and the Director of the Sensor Networks and Cellular

Systems (SNCS) Research Center, University of Tabuk. He coauthored papers in IEEE and other journals and conferences, and served on editorial boards and technical committees for many of them. His research interests include wireless communication, sensor networks, power systems, neurocomputing, and scientific visualization. He was a recipient of the IEEE Professor of the Year Award from UW. He was the Director of a laboratory that received the Boeing Supplier Excellence Award.